https://doi.org/10.5194/gmd-2022-104
Preprint. Discussion started: 19 July 2022

Geoscientific Model Development Discussions
Open Access

Basin-scale gyres and mesoscale eddies in large lakes: A novel procedure for their detection and characterization, assessed in Lake Geneva

Seyed Mahmood Hamze-Ziabari[1], Ulrich Lemmin[1], Frédéric Soulignac[1,2], Mehrshad Foroughan[1] and David Andrew Barry[1]

[1] Ecological Engineering Laboratory (ECOL), Environmental Engineering Institute (IIE), Faculty of Architecture, Civil and Environmental Engineering (ENAC), Ecole Polytechnique Fédérale de Lausanne (EPFL), 1015 Lausanne, Switzerland
[2] Commission Internationale pour la Protection des Eaux du Léman (CIPEL), Nyon, Switzerland

Correspondence to: Seyed Mahmood Hamze-Ziabari (mahmood.ziabari@epfl.ch)

Abstract. Gyres and eddies, i.e., large-scale rotating coherent water masses, are prominent features of large lakes and oceans, are formed due to the interplay between Coriolis force and wind stress. Understanding their dynamics is important as they are known to play a crucial role in spreading bio-chemical materials and energy throughout lakes and oceans. Since field observations in large lakes are sparse in time and location, often limited to a few moorings, they cannot provide a comprehensive validation dataset for such large-scale current systems. Previous numerical studies suggested the presence of different and complex gyre systems in many large lakes, however none were confirmed with detailed field measurements. In order to assess the spatial and temporal extent of gyres and eddies, their dynamics and vertical structure, as well as validate their prediction in numerical simulation results, transect field observations should be carried out. However, at present it is difficult to forecast when and where such transect field observations should be taken. To overcome this problem, a novel procedure combining 3D numerical simulations, statistical analyses, and remote sensing data was developed that permits determination of the spatial and temporal patterns of basin-scale gyres during different seasons. The efficiency and robustness of the proposed procedure was validated in Lake Geneva. For the first time in a lake, detailed field evidence of the existence of basin-scale gyres and (sub)mesoscale eddies was provided by data collected along transects whose locations were predetermined by the proposed procedure. The close correspondence between field observations and detailed numerical results further confirms the validity of the model for capturing large-scale current circulations as well as submesoscale eddies. The procedure can be applied to other large lakes and can be extended to the interaction of biological-chemical-physical processes.

1 Introduction

Pressure on large lakes, as major freshwater resources, is increasing due to a combination of changing climate and human activities. To a large extent, lake water quality is controlled by the pathways along which nutrients, phytoplankton and contaminants are transported/redistributed on meso- or basin-scales (Ralph, 2002); gyres and eddies play an important role in this current pattern. Basin-scale gyres are usually restricted in the vertical by the thermocline depth (Ishikawa et al., 2002; Ji

https://doi.org/10.5194/gmd-2022-104
Preprint. Discussion started: 19 July 2022

and Jin, 2006), which is also subject to high spatial and temporal variability due to the presence of mesoscale or submesoscale circulation (Nõges and Kangro, 2005; Ostrovsky and Sukenik, 2008; Corman et al., 2010).

Understanding gyre dynamics in large lakes has mainly been advanced by Csanady's theoretical analyses (Csanady, 1973, 1975). Wind forcing (the primary driver), the Earth's rotation (Coriolis force), and lakebed morphology are the main controlling parameters (Birchfield, 1967; Rao and Murty, 1970; Csanady, 1973; Pickett and Rao, 1977). In order to provide and accumulate enough energy to generate basin-scale circulation such as gyres, wind with a relatively constant direction must blow over most of the water surface for a certain time (Csanady, 1975). It has been shown that in the Laurentian Great Lakes in North America, a downwind flow in shallower nearshore regions and an upwind return flow in the deeper part of a lake basin enhance the formation of such circulation cells. Stratification and the width of downwind flow, which is also known as a "coastal jet", will increase and confine the flow to the surface layer (Bennett, 1974). However, these studies were conducted under simplified boundary conditions, using bathymetry and atmospheric forcing data with limited resolution.

Theoretical studies have indicated that the response of a depth-variable lake to a strong uniform wind often leads to the formation of two counter-rotating gyres, also known as a double-gyre or dipole (Csanady, 1973; Bennett, 1974; Shilo et al., 2007), as was confirmed by early numerical simulations (Simons, 1980). With increased computational power, three-dimensional (3D) hydrodynamic models with higher accuracy, stability and resolution have since been developed and have significantly contributed to the understanding of lake circulation, especially that driven by wind (e.g., Beletsky et al., 1999; Laval et al., 2005; Beletsky and Schwab, 2008; Bai et al., 2013; Mao and Xia, 2020; Baracchini et al., 2020; Lin et al. 2022; Wu et al. 2022). Recent numerical simulations have also highlighted the role of baroclinicity induced by gradients of surface buoyancy (mainly surface heating and cooling), which can enhance the large-scale circulation in the Great Lakes (Schwab and Beletsky, 2003; Bennington et al., 2010; Verburg et al., 2011; McKinney et al., 2012).

Based on long-term current data of the Laurentian Great Lakes from a limited number of moorings, Beletsky et al. (1999) suggested that during the non-stratified season, a single counterclockwise rotating gyre exists in the larger lakes (Lake Huron, Lake Michigan, Lake Superior), whereas a two-gyre pattern is established in the smaller ones (Lake Ontario, Lake Erie). Stratification may modify this pattern. A two-gyre pattern was also observed in Lake Okeechobee (USA), a shallow (3.2 m mean depth) large lake (Ji and Jin, 2006). In Lake Biwa (Japan), topography, stratification and non-linearity were found to affect gyre development and could result in a three-gyre pattern (Akitomo et al., 2004). Determining the direct influence of atmospheric forcing on individual large-scale current systems in large lakes is quite challenging due to the complexity and potential range of hydrodynamic responses.

In parallel to increased computational capacity, high-resolution satellite images allow direct observations of gyres and mesoscale and submesoscale eddies (Steissberg et al., 2005; Zhan et al., 2014). In particular, Synthetic Aperture Radar (SAR) imagery is applied to detect and characterize eddies in oceans (e.g., Johannessen et al., 1996; DiGiacomo and Holt, 2001; Marmorino et al., 2010; Qazi et al., 2014). Although small coastal cyclonic eddies were identified in Lake Superior with SAR imagery (McKinney et al., 2012), it has not yet been used to detect basin-scale gyres in lakes.

https://doi.org/10.5194/gmd-2022-104
Preprint. Discussion started: 19 July 2022

Numerical simulations of large-scale motions in Lake Geneva (e.g., Umlauf and Lemmin, 2005; Perroud et al., 2009; Le Thi et al., 2012; Razmi et al., 2013; Cimatoribus et al., 2018, 2019; Baracchini et al., 2020; Reiss et al., 2020) show that the Coriolis force is important in the force balance, and that gyres form. Although the existence of different gyre systems was suggested by these studies, none were confirmed with detailed field measurements. Based on long-term mooring data, albeit limited, Lemmin and D'Adamo (1996) suggested the existence of a basin-scale gyre. The formation of smaller scale eddies in two embayments was observed, affected by the embayment geometry (Razmi et al., 2013) and by meteorological conditions (Razmi et al., 2017).

In past studies, numerical modeling results and observations from moored current meters were analyzed for the presence of large-scale gyres mainly by studying individual events. However, since field observations in large lakes are generally sparse in time and space, often limited to a few moorings, they cannot provide a detailed description of the large-scale gyre pattern (Beletsky et al., 2013; Hui et al., 2021) and, in particular, determine whether these patterns are "typical" and thus important in the long-term development of the lake flow system. Therefore, in order to improve the understanding of the general circulation in large lakes, an algorithm that allows identifying and tracking basin-scale and mesoscale water mass movements in a lake is needed. In this context, one of the most popular methods in oceanography to identify and track eddies from Sea Level Anomaly maps and numerical modeling results is based on the Okubu-Weiss (OW) parameter (e.g., Isern-Fontanet et al., 2004; Xiu et al., 2010; Chang and Oey, 2014). The OW parameter allows separation of flow fields into vorticity-dominated regions (gyres and eddies) and strain-dominated regions (the ambient flow field) (Okubo, 1970; Weiss, 1991).
In the present study, high-resolution 3D hydrodynamic model results from Lake Geneva are combined with the OW parameter and Empirical Orthogonal Function (EOF) analysis in a novel procedure with the following objectives:

(i) To detect large-scale coherent flow features in large lakes, in particular large-scale gyres and mesoscale eddies.
(ii) To design strategies for field campaigns that can confirm the existence of these features and thus, for the first time, provide unambiguous detailed field evidence of basin-scale gyres and mesoscale eddies in lakes.
(iii) To identify links between atmospheric forcing patterns and the dominant variability of basin-scale flow systems that can help to predict the occurrence and the lifetime of the dominant flow patterns.

The Supplementary Information (SI) section provides additional figures, tables, and clarifications and details, denoted with prefix S.

2 Materials and Methods

2.1 Study site

Lake Geneva (*Lac Léman*), the largest lake in Western Europe, is a crescent-shaped pre-alpine lake, situated between Switzerland and France (Figure 1). It is composed of an eastern basin, the *Grand Lac*, with a maximum depth of 309 m and a western shallow and narrow basin, the *Petit Lac*, with a maximum depth of nearly 70 m. The lake is approximately 70-km long, has a maximum width of 14 km, a surface area of 580 km^2 and a volume of 89 km^3. The lake is located between the Alps

https://doi.org/10.5194/gmd-2022-104
Preprint. Discussion started: 19 July 2022

to the south and east, and the Jura to the northwest. Two strong, dominant wind fields, namely the *Bise* (coming from the northeast) and the *Vent* (coming from the southwest), are guided by the surrounding topography (Wanner and Furger, 1990; Lemmin and D'Adamo, 1996). The central and western parts of the lake can experience strong wind events, which may last from several hours to several days. The eastern part of the lake is sheltered from strong wind events by the surrounding high mountains (Rahaghi et al., 2018; Lemmin, 2020).

Coriolis force plays an important role in the formation of gyres, since the width of the lake is much larger than the internal Rossby radius of deformation; the typical range of the Rossby radius is O(5 km) during strongly stratified seasons, and O(1 km) during weakly stratified seasons (Lemmin and D'Adamo, 1996; Cimatoribus et al., 2018). Numerical simulations show that basin-scale gyres in Lake Geneva can rotate clockwise (anticyclonic) or counterclockwise (cyclonic) due to the surrounding topography and the two dominant wind fields, *Bise* and *Vent* (Figure 1a) (Razmi et al., 2017; Cimatoribus et al., 2018, 2019).

Lake Geneva is well suited for studying gyre dynamics and testing the new procedure, since it exhibits the full range of hydrodynamic complexity expected in a large, oligomictic lake with a strong summer and weak winter stratification; occasional full convective mixing only occurs during exceptionally cold winters. Furthermore, all background data needed for the development of this procedure are available in the public domain.

https://doi.org/10.5194/gmd-2022-104
Preprint. Discussion started: 19 July 2022

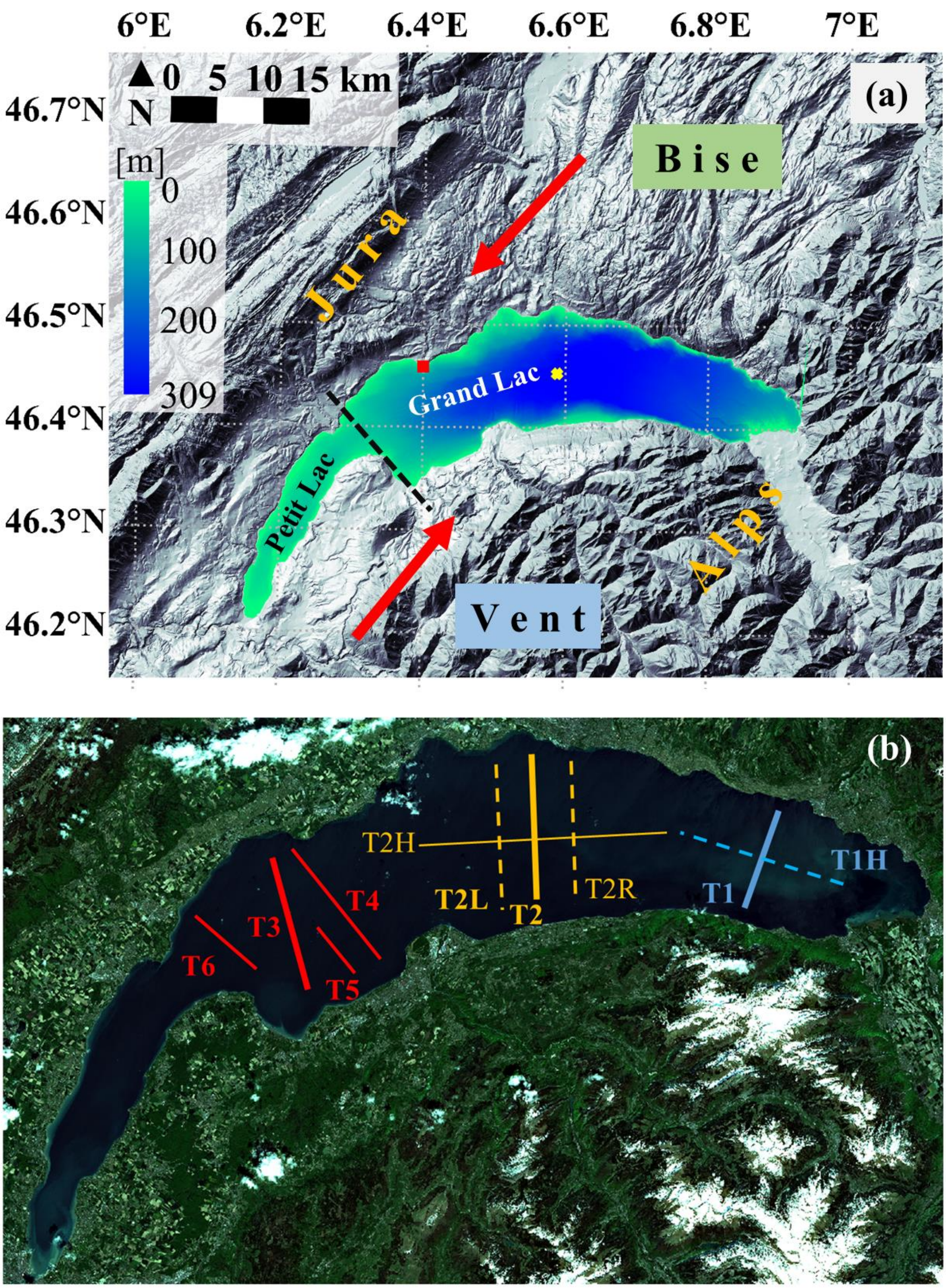

https://doi.org/10.5194/gmd-2022-104
Preprint. Discussion started: 19 July 2022

Geoscientific Model Development Discussions
Open Access EGU

Figure 1. (a) Lake Geneva and surrounding topography, adapted from a public domain satellite image (NASA World Wind, last accessed 2 August 2019) and bathymetry data from SwissTopo (last accessed 2 August 2019). The colorbar indicates the water depth. SHL2 (yellow cross) is a long-term CIPEL monitoring station where data on physical and biological parameters are measured. The red square shows the location of the EPFL Buchillon meteorological station (100-m offshore). The black dashed line approximately delimits the two basins of Lake Geneva called the *Petit Lac* and the *Grand Lac*. The thick red arrows indicate the direction of the two strong dominant winds, called the *Bise* (coming from the northeast) and the *Vent* (coming from the southwest). (b) A schematic view of transects (T) selected for the different field campaigns in this study (see text and Table S1 in SI for details). The background satellite image is taken from Sentinel-1A.

2.2 Hydrodynamic modeling

In this study, MITgcm (Marshall et al., 1997), which solves the 3D Boussinesq, hydrostatic Navier-Stokes equations (including the Coriolis force), was used in a series of numerical simulations for Lake Geneva for 2018 and 2019, based on the model setup of Cimatoribus et al. (2018). The model was forced by meteorological data (wind fields, atmospheric temperature, humidity, solar radiation) extracted from the COnsortium for Small-scale MOdeling (COSMO) atmospheric model of MeteoSwiss (last accessed 6 June 2021) (Voudouri et al., 2017). The first modeling step was a Low Resolution (LR) model (horizontal resolution 173 to 260 m, 35 depth layers, integration time step 20 s), which was initialized from rest using the temperature profile from CIPEL station SHL2 (CIPEL, 2019) measured on 25 October 2017 and 19 December 2018, respectively (calm weather conditions prevailed on both dates). For each run, the LR model spin up was ~180 d. The 3D interpolated results of the LR modeling were then used to initialize the High Resolution (HR) version of the model (horizontal resolution 113 m and 50 depth layers, with layer thicknesses ranging from 0.30 m at the surface to approximately 12 m for the deepest layer, integration time step of 6 s). For each year, the HR model was run for two seasons: under weakly stratified conditions and under strongly stratified conditions.

The model's capability to realistically reproduce stratification, mean flow, and internal seiche variability in Lake Geneva was demonstrated by Cimatoribus et al. (2018, 2019). To further assess the model's ability to reproduce seasonal stratification, a separate validation was carried out in the present study using temperature profiles measured in 2019 at SHL2 (Figure S1 in SI), located at the center of the *Grand Lac* (Figure 1a).

2.3 Transect field measurements

Based on the proposed procedure, six transects were selected in different parts of the *Grand Lac* (Figure 1b), i.e., one transect in the eastern part, and five in the central and western parts (details below). The large-scale gyre in the central part of the *Grand Lac* was the main focus of the transect field measurements due to its importance and persistence. Along each transect, ten profiles of current velocity spaced 1 km apart were measured, each for at least 10 min using an Acoustic Doppler Current Profiler (ADCP, Teledyne Marine Workhorse Sentinel) with the transducer located at 0.5-m depth. The ADCP was equipped

https://doi.org/10.5194/gmd-2022-104
Preprint. Discussion started: 19 July 2022

with a bottom-tracking module, was set up for 100 1-m bins (blanking distance of 2 m), and operated in high-resolution processing mode. Tilt and heading angles were derived from sensors located inside the instrument.

2.4 SAR remote sensing

Synthetic Aperture Radar (SAR) is frequently used to detect oceanic surface features under light wind conditions (Johannessen et al., 1996; Wang et al., 2019). The main advantages of SAR imagery are that: (i) it functions day and night under all weather conditions, (ii) it has high sensitivity to small scale variability of the water surface, and (iii) it provides high resolution images. The patterns observed in SAR images are due to the change of water surface roughness, which is influenced by wave/current interactions, natural surface films and spatial variations of the local wind field (Johannessen et al., 2005). Gyres or eddies in SAR images are indicated by dark spiral features called "black" or "classical" eddies (Karimova, 2012). More details are given in the section S1 in SI. For the present study, C-band SAR data were obtained from the European Space Agency's (ESA) Sentinel-1A and Sentinel-1B satellites. The co-polarized VV (Vertical transmit, Vertical receive SAR polarization) data were used because noise restricts the application of VH (Vertical transmit, Horizontal receive SAR polarization) data (Gao et al., 2019). The spatial resolution of SAR data varies between 5 and 20 m for a ground sampling distance of 10 m.

2.5 Okubo-Weiss parameter and Empirical Orthogonal Functions

The Okubo-Weiss (OW) parameter describes the local strain-vorticity balance in the horizontal flow field of a shallow fluid layer. It allows separating vorticity-dominated regions associated with basin-scale gyres or mesoscale eddies from strain-dominated ambient regions (Okubo, 1970; Weiss, 1991) and can be written as:

$$\mathrm{OW} = S_n^2 + S_s^2 - \omega_z^2 \quad (1)$$

where S_n is the normal component of strain, S_s is the shear component of strain, and ω_z is the relative vorticity of the flow, defined respectively by:

$$S_n = \frac{\partial u}{\partial x} - \frac{\partial v}{\partial y} \quad (2)$$

$$S_s = \frac{\partial v}{\partial x} + \frac{\partial u}{\partial y} \quad (3)$$

$$\omega_z = \frac{\partial v}{\partial x} - \frac{\partial u}{\partial y} \quad (4)$$

where (u,v) are Cartesian components of the horizontal flow field at different depths and times.

For a given data set, EOF analysis identifies the main spatial patterns (E) and their temporal evolution (P) (Wang and An, 2005). Hourly-averaged OW values derived from numerical simulations were decomposed into the basis function $E_{\mathrm{OW}}^k(X)$ and the principal component coefficient $P_{\mathrm{OW}}^k(t)$ as:

$$\mathrm{OW}(X,t) = \sum_{k=1}^{N} E_{\mathrm{OW}}^k(X) P_{\mathrm{OW}}^k(t) \quad (5)$$

where k is the EOF mode, which varies from 1 to the maximum N, $X = (x,y)$ is the position under consideration and t is time. The $E_{\mathrm{OW}}^k(X)$ modes identify the spatial patterns of the OW parameter. The time evolution of each $E_{\mathrm{OW}}^k(X)$ mode can be obtained from the time series of principal component coefficients, indicated as $P_{\mathrm{OW}}^{k}(t)$. Positive OW values relate to strain-dominated regions, whereas negative OW values identify vorticity-dominated regions.

3 Procedure for detecting gyres

The proposed gyre identification procedure consists of four steps (Figure 2): (i) data pre-processing, (ii) extracting dominant patterns using EOF analysis of OW fields, (iii) defining the 3D structure of a gyre, and (iv) finding the correlation between the dominant gyre pattern and environmental forcing.

In step (i), the OW values are computed for selected time windows using the horizontal velocity fields (u,v) generated by the 3D numerical modeling. Vorticity-dominated and strain-dominated regions can be identified from OW values, and can then, for step (ii), be used to locate and characterize the gyre flow field, in particular, gyre centers and the outer limits of gyres, located where vorticity and strain are approximately in balance. This is further supported/confirmed by patterns detected in SAR images. This OW/EOF analysis is repeated for several depths in step (iii), in order to verify that this surface pattern documents a gyre extending over the upper layers with its depth limited by the thermocline. Step (iv) links the observed dominant OW pattern to the forcing which generated it, thereby identifying forcing patterns, mainly wind events, preceding the formation of gyre patterns. Scrutinizing actual meteorological data for such forcing patterns will then allow planning when and where to take detailed transect field measurements of the gyre pattern in the lake.

3.1 Detection of the core of a gyre or eddy

The separation of the OW field in terms of its sign can be used to detect cores of complex fluid flows (McWilliams, 1984; Elhmaïdi et al., 1993). These cores are characterized by negative OW values below a given (negative) threshold, OW_T (Pasquero et al., 2001; Isern-Fontanet et al., 2006; Henson and Thomas, 2008; Liu et al., 2021). For this purpose, a threshold value of $\mathrm{OW}_T = 0.2\sigma_{ow}$ was defined, where σ_{ow} is the root-mean-square fluctuation of OW in the epilimnion with the same sign of the vorticity of the gyre/eddy core (Pasquero et al., 2001; Isern-Fontanet et al., 2006; Henson and Thomas, 2008).
In the data pre-processing stage, the hourly computed OW values were normalized by hourly values of OW_T such that the normalized OW parameter, OW_N, partitions the topology of the gyre/eddy field into three regions: elliptic regions, $\mathrm{OW}_\mathrm{N} < -1$, hyperbolic regions, $\mathrm{OW}_\mathrm{N} > 1$, and a background field, $|\mathrm{OW}_\mathrm{N}| \leq 1$ (Pasquero et al., 2001; Isern-Fontanet et al., 2006). As shown in Figure 2, elliptic regions, which represent the center of gyres/eddies, are significantly more pronounced than the other regions. In lakes, basin-scale gyres are mainly restricted by the lake basin geometry and also impacted by the surrounding topography. Therefore, the regions with $\mathrm{OW}_\mathrm{N} > -1$ can be influenced by the interaction between gyres and nearshore boundaries. As a result, a wide spatial variability in the OW_N values for these regions was observed, whereas regions with $\mathrm{OW}_\mathrm{N} < -1$ were spatially rather stable. To eliminate such processes from the spatial and temporal identification of gyres/eddies, the regions with $\mathrm{OW}_\mathrm{N} > -1$ were filtered before implementing the EOF analysis.

For the proposed procedure (Figure 2), hourly filtered OW_N values of different depth layers were computed for each month. The EOF analysis was then applied to detect the main modes (spatial pattern) and the corresponding principal

https://doi.org/10.5194/gmd-2022-104
Preprint. Discussion started: 19 July 2022

component time series. From different modes of the EOF results, signatures of gyre or eddy cores were identified based on the following criteria:

1. A local extreme value exists in the spatial modes of OW_N values
2. At least one closed line exists around each local extreme value
3. The core edge is identified as the closed line where the sign of $E_{OW_N} \times P_{OW_N}$ changes
4. A vertical and horizontal coherence of a gyre or eddy signature must exist between different depth layers (bounded below by the thermocline), i.e., criteria 1-3 above must be spatially consistent for different depth layers.

By applying these criteria, the location of gyre and eddy centers can be identified.

3.2 Detecting the outer boundary of a gyre or an eddy

Gyre boundaries are located where vorticity and strain are approximately in balance, i.e., $|OW_N| \leq 1$. However, as discussed above, the outer gyre boundaries cannot be completely resolved by the OW analysis. Furthermore, the noise in the resulting fields of OW_N makes the detection of coherent flow structures difficult (Souza et al., 2011). Defining vertical and horizontal coherence criteria that can confirm the coherent 3D pattern of gyres can significantly reduce this limitation of the OW parameter analysis. This threshold-based boundary detection method can be complemented by a geometry-based method using contour lines in Synthetic Aperture Radar (SAR) images. Since basin-scale gyres and large eddies can be detected in SAR images, information about the outer boundaries in support of the OW_N analysis results can be obtained from SAR imagery.

3.3 Finding the link between the temporal variation of a gyre and environmental forcing

Wind stress and surface buoyancy flux (due to heating/cooling) are the processes controlling gyre circulations and their variability. To find a link between the pattern of external forcing and the computed spatial pattern of the OW_N parameter presented in the previous sections, monthly EOF analyses of the total wind stress ($\sqrt{\tau_x^2 + \tau_y^2}$) and the net upward heat flux extracted from the COSMO atmospheric data are implemented. In the final stage of the procedure, the lagged cross-correlations between the spatial mode and the corresponding principal component time series of the environment forcing and the OW_N are examined.

https://doi.org/10.5194/gmd-2022-104
Preprint. Discussion started: 19 July 2022

Geoscientific Model Development
Discussions

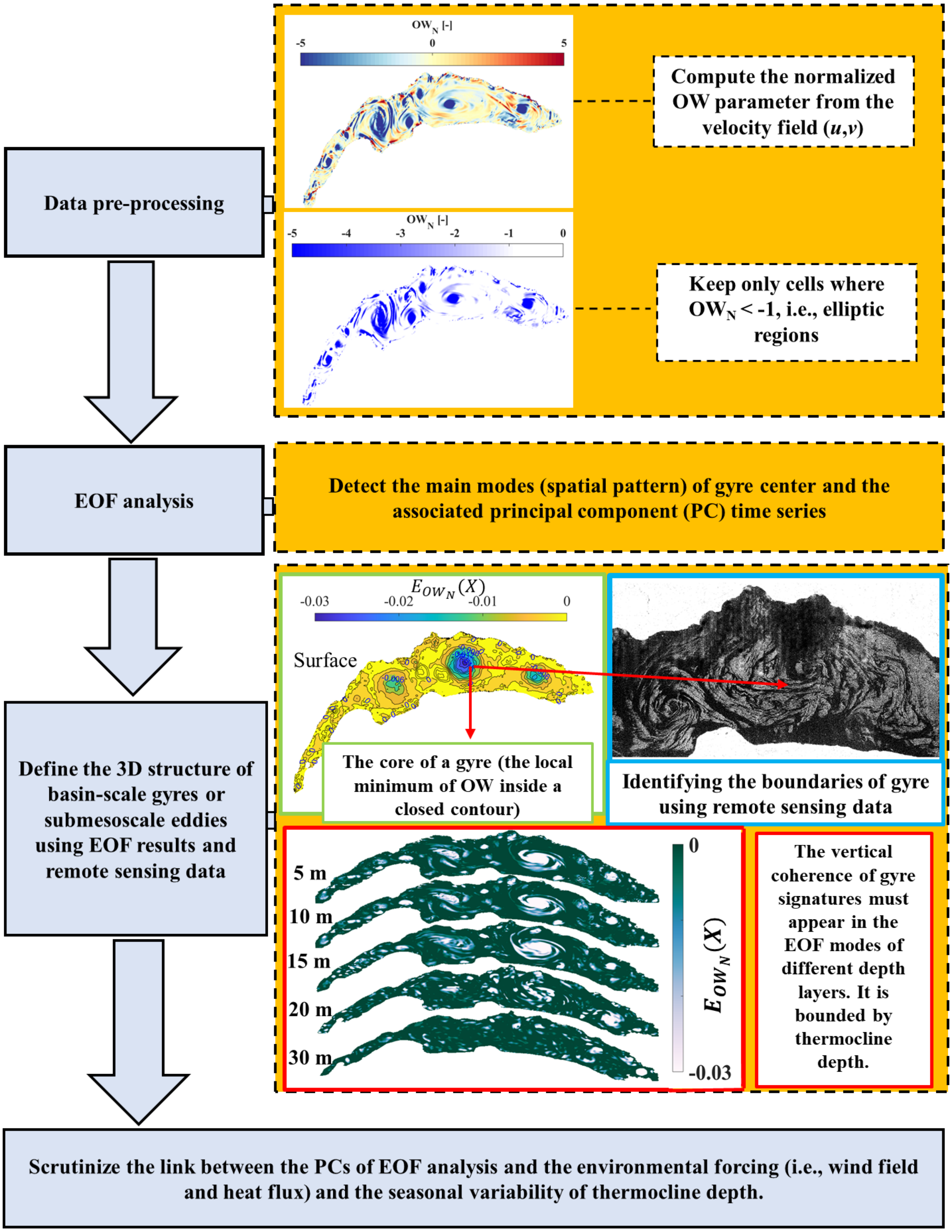

Figure 2. Flowchart of the proposed procedure for detecting basin-scale gyres and eddies applied to Lake Geneva.

https://doi.org/10.5194/gmd-2022-104
Preprint. Discussion started: 19 July 2022

Geoscientific Model Development Discussions
Open Access EGU

4 Results

In this section, the performance of the procedure for detecting the temporal and spatial variations of gyres/eddies is first evaluated for September 2018. Thereafter, the robustness of the proposed procedure is assessed by comparing results of transect field campaigns that were carried out based on the proposed procedure with numerical results during weakly and strongly stratified months.

4.1 Detecting gyres and eddies: Okubo-Weiss parameter and EOF analysis

4.1.1 Detection of the location of gyre centers

Results of numerical 3D modeling for the month of September 2018 are used to demonstrate the performance of the proposed procedure. The first and second modes of the OW_N variations in different depth layers (1, 5, 10, 15, 20 and 30 m) are given in Figures 3a,b. Due to the quick convergence of the EOF decomposition modes, only the first two dominant EOF modes are analyzed for detecting elliptic regions with negative OW_N values. The first mode dominates the overall OW_N variations, since it accounts for nearly 56% of the total variance down to 15 m depth, and ~47% for deeper depths. The second mode contributes nearly 23 % to the total variance for the near surface layers and the remaining modes, which each contains less than 5% of the total variance, are not presented here.

Three closed trajectories that encircle regions with negative $E_{\mathrm{OW_N}}$ values can be distinguished in the first mode at different depth layers (Figure 3a). It should be noted that these regions can indicate the presence of three large-scale gyres in the *Grand Lac*, if $E_{\mathrm{OW_N}} \times P_{\mathrm{OW_N}} < 0$ (the time series of $P_{\mathrm{OW_N}}$ are discussed in the following sections). The location of the center of each gyre in different depth layers is calculated by averaging the coordinates of the gyre centers (based on criteria 1-3 as discussed above). The closed trajectories weaken with depth down to 20 m and disappear at 30-m depth due to the presence of the thermocline, which is situated ~15-m depth.

A region bounded by closed trajectories with negative OW_N can also be considered as an indicator for areas where pelagic upwelling or downwelling are more likely to occur. Details of the spatial OW_N pattern (e.g., Figure 4c, d) confirm the presence of negative OW_N regions in the center of the large-scale gyres. The rotation sign of the three-gyre pattern after the *Bise* event is given in Figures S5, S6, and S7 for different months. The Anticyclonic Gyre (clockwise rotating) in the west and two Cyclonic Gyres (counterclockwise rotating) in the center and in the east are hereinafter referred to as AG, CG1, and CG2, respectively (Figure 3a). The second EOF mode reveals the simultaneous existence of smaller eddies, often with shorter lifetimes than basin-scale gyres (Figure 3b). More details on these eddies are presented below.

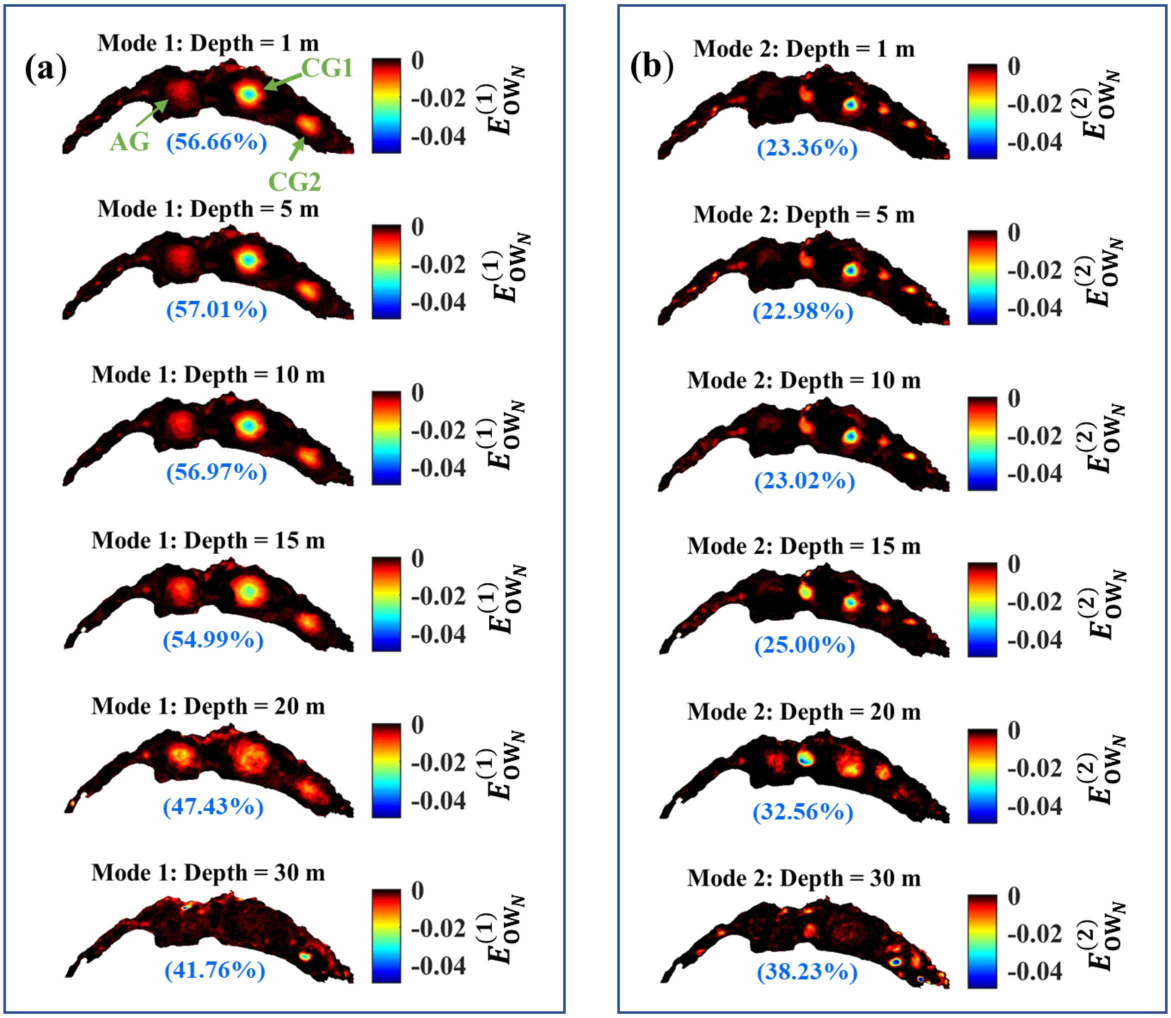

Figure 3. EOF analysis of the MITgcm output for Lake Geneva for the month of September 2018: (a) First and (b) second modes of EOF of the normalized OW_N parameter are shown for different depth layers. The first mode is dominated by three large-scale gyres (circular zones of negative OW_N values), whereas in the second mode, (sub)mesoscale eddies also appear. Colorbars give the range of the EOF.

4.1.2 Detection of the outer boundary of a gyre or an eddy

The OW_N analysis shows that gyre centers have strongly negative OW_N values and that positive OW_N areas surround the gyres (Figure 4b, d). The transition zone between the two zones ($|OW_N| \leq 1$), which should indicate the outer edge of the gyre, is wide in certain parts of the circumference and does not allow determining the outer edge of the gyre (Figure 4b, d). SAR images may be used to confirm/define this edge (more details in S1). The boundaries between the two Cyclonic Gyres in the

https://doi.org/10.5194/gmd-2022-104
Preprint. Discussion started: 19 July 2022

eastern part of lake, i.e., CG1 and CG2, can be determined from SAR data obtained from Sentinel-1 on 21 July and 12 October 2018 (Figure 4a, c), where two (elliptical) gyres are evident. The minor/major axes of CG1 and CG2 are approximately 6.5/12.9 and 9.8/15.9 km, respectively. Smaller eddies, marked by strong negative OW_N values in their center surround the large-scale CG1 and CG2 gyres.

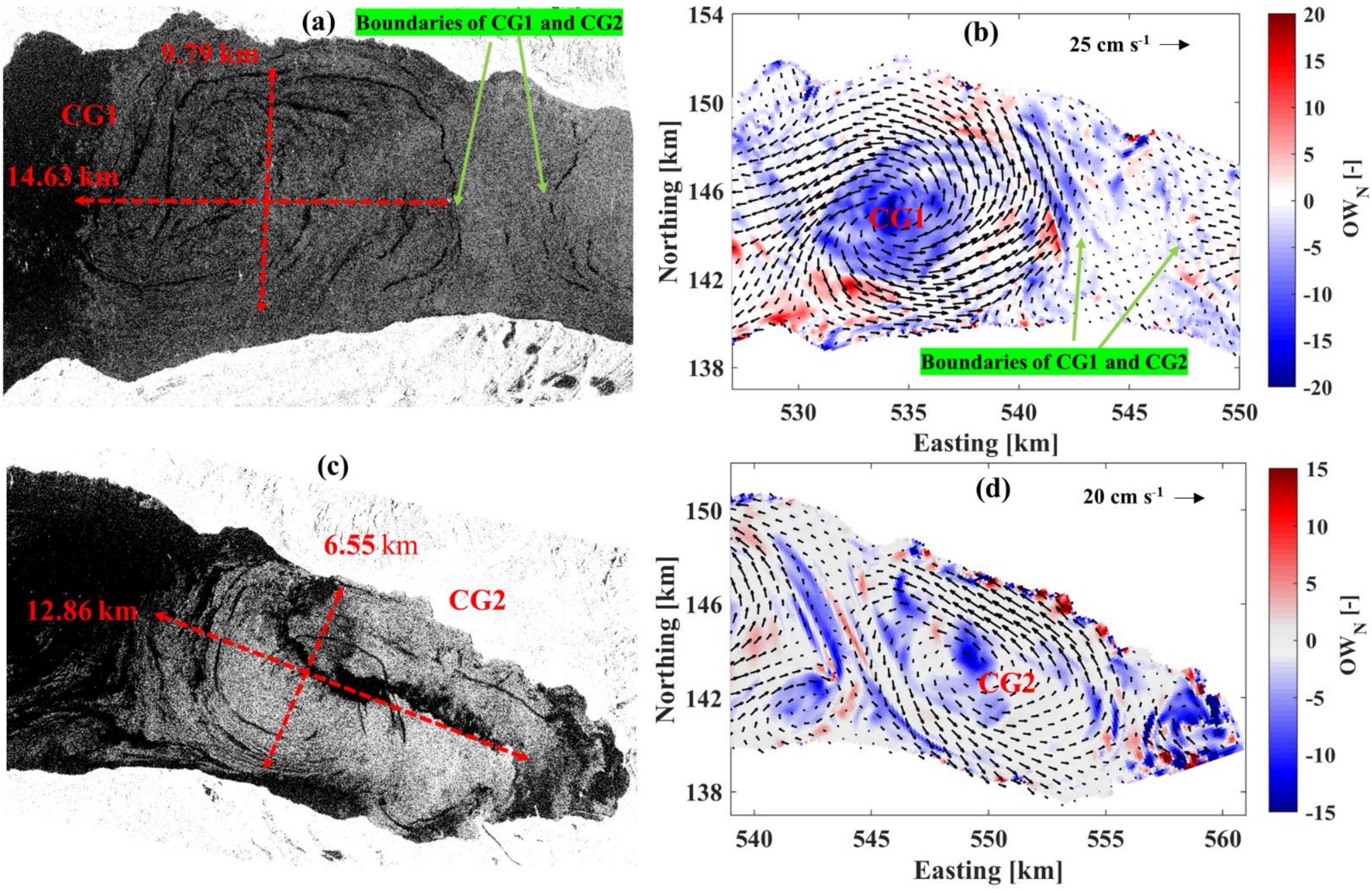

Figure 4. Remote sensing evidence (SAR images, Sentinel-1) of two Cyclonic Gyres (CG) in the eastern part of Lake Geneva: (a) CG1 for 21 July 2018 and c) CG2 for 12 October 2018. Red dashed lines indicate the dimensions of the gyres. Panels (b) and (d): Corresponding modeled surface velocity fields (small black arrows show sense of rotation) and OW_N parameter values shown by colors. Strong negative OW_N parameter values (blue) indicate the location of core zones of large-scale gyres and mesoscale eddies. The colorbars give the range of the OW_N values.

4.1.3 Detecting large-scale gyres: Link between environmental forcing and gyre signature

To find a link between the pattern of external forcing and the computed spatial pattern of the OW_N parameter, EOF analyses of the total wind stress and the net upward heat flux extracted from the COSMO atmospheric data for September 2018 were

https://doi.org/10.5194/gmd-2022-104
Preprint. Discussion started: 19 July 2022

carried out. The first spatial mode and the corresponding principal component time series of the total wind stress ($c_w^{(1)}(x)$, $\varphi_w^{(1)}(t)$) and the upward heat flux ($c_{HF}^{(1)}(t)$, $\varphi_{HF}^{(1)}(t)$) are presented in Figures 5a, b, respectively. The first mode of the external forces dominates the variation of the forces, since it constitutes ~98% and 99% of the total variance related to the total wind stress and heat flux, respectively. The total variance differences between the first spatial modes and the principal component time series obtained from the solution with two dominant modes and the solution with all possible modes is negligible (O(10^{-10}-10^{-14})) compared to the calculated absolute values (O(10^{-3})) (Figure S2).

The EPFL Buchillon field station (Figure 1b) data show that a strong *Bise* event started at ~00:00 on 24 September 2018 and ended at ~11:00 on 26 September 2018. The mean wind speed ±1 standard deviation was 4.21 ± 1.88 m s^{-1} with wind gusts of 8.40 ± 3.37 m s^{-1}. The mean wind direction was 61 ± 13° (Figure 5c, d). Figure 5e suggests that there is a link between the strong *Bise* event and the first EOF mode of OW_N indicated by the principal component ($P_{OW_N}^{(1)}(t)$) time series. To determine this link, lagged cross-correlations were computed between the principal component time series of the dominant EOF modes of atmospheric forcing, i.e., the total wind stress ($\varphi_w^{(1)}(t)$) and the net upward heat flux, ($\varphi_{HF}^{(1)}(t)$), and the two dominant EOF modes of OW_N (Figure 6). The lagged cross-correlation between the upward heat flux and $P_{OW_N}^{(1)}(t)$ does not exceed 0.3 in the depth layers influenced by the gyres (i.e., 2-20 m; Figure 3). On the other hand, the cross correlation between $\varphi_w^{(1)}(t)$ and $P_{OW_N}^{(1)}$ reaches values > 0.8 in the same depth layers and a positive peak with a lag of 1-1.5 days for the near surface layers (1-20 m; Figure 6a-f). A positive peak means that $\varphi_w^{(1)}(t)$ and $P_{OW_N}^{(1)}(t)$ have the same sign. These results imply that the three-gyre pattern in the first mode (Figure. 3a) is predominantly controlled by the spatial and temporal variations of wind stress, i.e., $c_w^{(1)}(x)$ and $\varphi_w^{(1)}(t)$. Furthermore, the time series of the first mode, $P_{OW_N}^{(1)}(t)$, in different depth layers suggest that the three-gyre pattern can persist for several days (nearly 5 days) after the wind peak (Figure 5e).

Thereafter (29 September 2018), the large-scale gyres break down into smaller gyres/eddies, and the second mode of OW_N dominates (Figure 5f). The cross-correlation between wind stress, upward heat flux and $P_{OW_N}^{(2)}(t)$ is not greater than 0.35 in the depth layers influenced by the gyres (Figure 6g-l). For wind stress, $E_{OW_N}^{(2)}$ is excited with a lag of ~ 5.5 days, with the same sign, and for upward heat flux with a lag of more than 4 days, again, with the same sign. Moreover, negative peaks in the cross-correlation between $E_{OW_N}^{(2)}$ and $\varphi_{HF}^{(1)}(t)$ show that $E_{OW_N}^{(2)}$ can be excited with a lag of 1-2 days, due to differential heating and cooling during day-night cycles (Figure 6g-l). However, $E_{OW_N}^{(2)}$ is only weakly excited by wind stress or upward heat flux. In addition to the effects of environmental forcing presented above, the basin shape and bathymetry also change the gyre pattern over time.

https://doi.org/10.5194/gmd-2022-104
Preprint. Discussion started: 19 July 2022

Geoscientific Model Development
Discussions

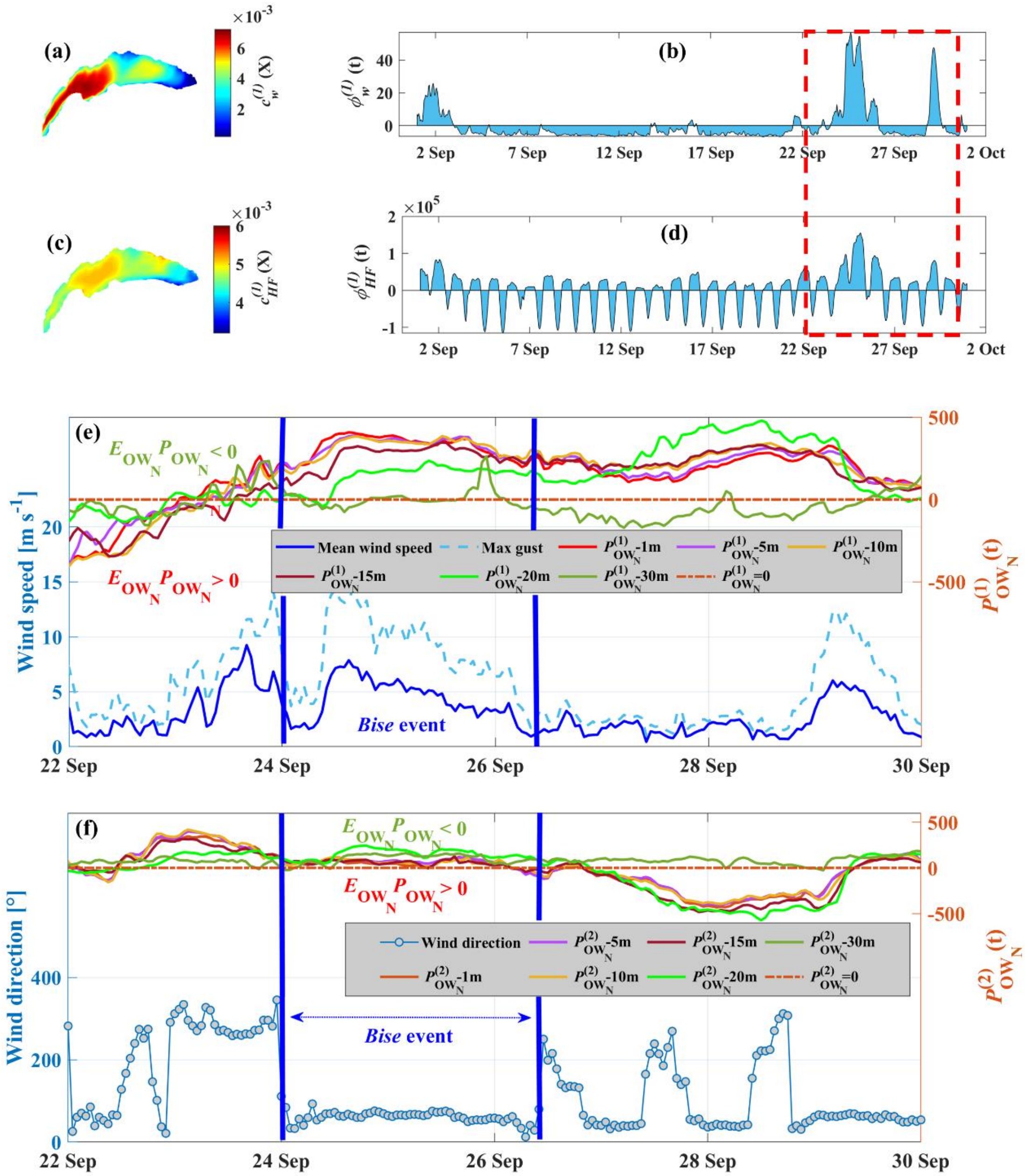

Figure 5. For September 2018: (a) First spatial mode ($c_w^{(1)}(X)$) and (b) principal component time series ($\varphi_w^{(1)}(t)$) of the total wind stress. (c) First spatial mode $c_{HF}^{(1)}(X)$ and (d) principal component time series ($\varphi_{HF}^{(1)}(t)$) of the net upward heat flux. (e) Mean wind speed and wind gusts at the Buchillon station (see Fig. 1 for location) for the period indicated by the red dashed-lined box in (b) and (d), and the principal component time series of the OW_N parameter associated with the first spatial mode ($P_{OW_N}^{(1)}(t)$) in different depth layers. (f) Wind direction at the Buchillon station for the period indicated by the red dashed-lined

https://doi.org/10.5194/gmd-2022-104
Preprint. Discussion started: 19 July 2022

Geoscientific Model Development
Discussions
Open Access

box in (b) and (d),, and the principal component time series of the OW_N parameter associated with the second spatial mode ($P^{(2)}_{OW_N}(t)$) at different depth layers. Colorbars in (a) and (c) show the range of the parameters. The colors in the legends of the two lowest panels correspond to the different depths. In (e) and (f), negative ($E_{OW_N}P_{OW_N}$) indicates the negative regions of OW_N parameter (the elliptic regions) and the presence of gyres.

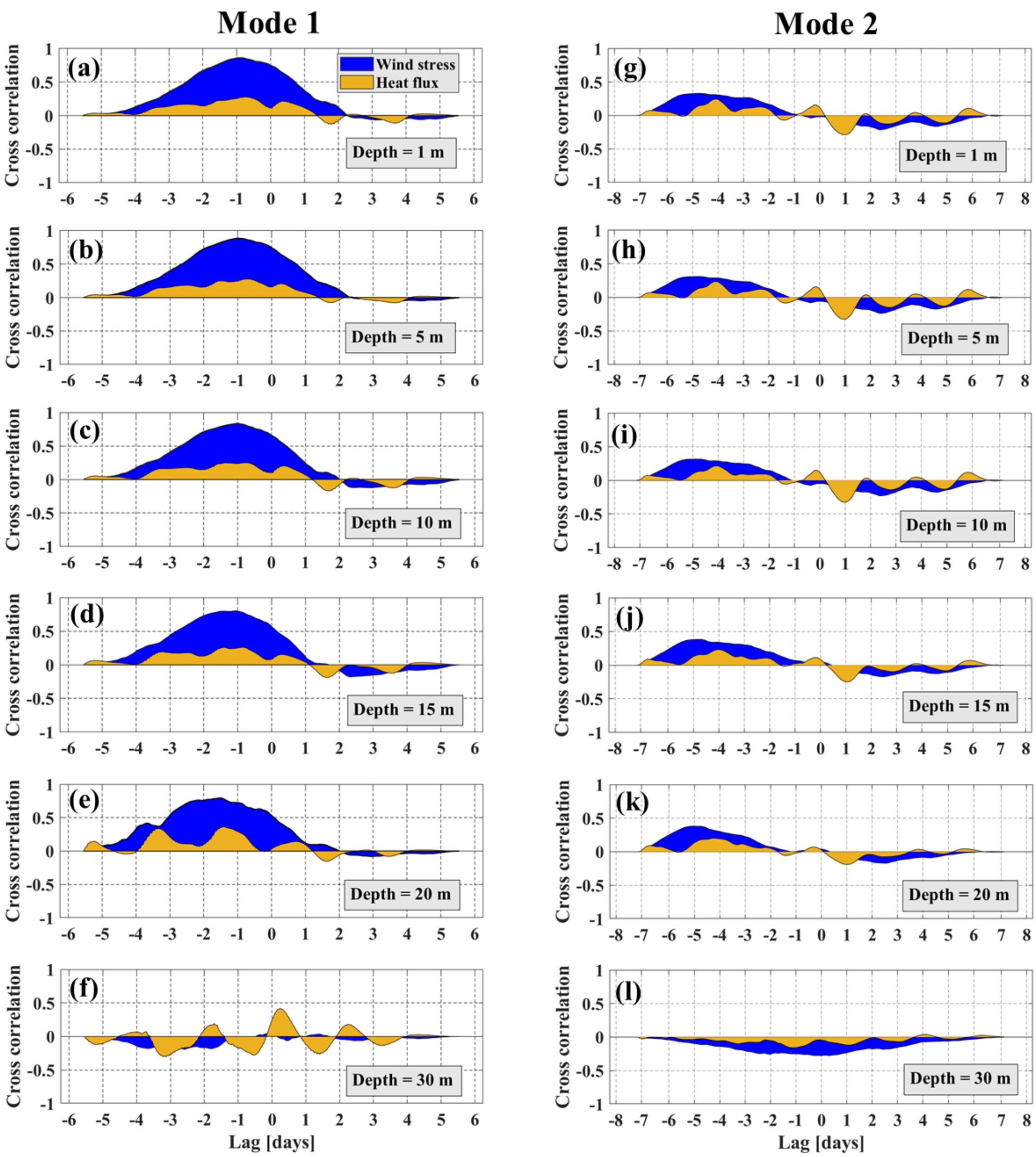

Figure 6. (a)-(f) Lagged cross-correlation of the principal component time series of the total wind stress ($\varphi^{(1)}_{w}(t)$) and the net upward heat flux ($\varphi^{(1)}_{HF}(t)$) with the principal component time series of the OW_N parameter associated with the first spatial

https://doi.org/10.5194/gmd-2022-104
Preprint. Discussion started: 19 July 2022

mode ($P^{(1)}_{\mathrm{OW}_N}(t)$) in different depth layers (depths are indicated). (g)-(l) Lagged cross-correlation of the principal component time series of the total wind stress ($\varphi^{(1)}_w(t)$) and the net upward heat flux ($\varphi^{(1)}_{HF}(t)$) with the principal component time series of $\mathrm{OW_N}$ the parameter associated with the second spatial mode ($P^{(2)}_{\mathrm{OW}_N}(t)$) in different depth layers.

4.2 Detecting large-scale gyres: Transect field campaigns

4.2.1 A cyclonic gyre at the center of the *Grand Lac* basin

To validate the proposed procedure for detecting the location and time of basin-scale gyres after a strong wind event, a field measurement campaign was planned for September 2019 and focused on capturing the largest basin-scale gyre, CG1, in the central part of the *Grand Lac* basin (Figures 3, 4). Buchillon field data recorded a strong *Bise* event that started on 17 September 2019 at ~20:00 and ended on 20 September 2019 at ~13:00 (mean wind speed ±1 standard deviation was 3.65 ± 0.86 m s^{-1}, with gusts of 7.69 ± 1.78 m s^{-1} and mean wind direction of 64 ± 11°). Furthermore, the spatial pattern of total wind stress computed from the forecasted COSMO atmospheric data (Figure S3) also revealed the same spatial pattern as observed for the September 2018 *Bise* event discussed above. For September 2018, it was shown that the three-gyre system pattern is highly correlated with strong *Bise* events (Figures 5 and 6). This pattern forms and persists for several days after the wind event has ceased. Therefore, based on these results, a field campaign was designed to capture the boundary and temporal variation of CG1 from 20 to 22 September 2019.

Four transects, T2, T2L, T2R, and T2H (see Figure 1b; coordinates are given in Table S1 in SI) were chosen to investigate the 3D structure of CG1 and its evolution. A few hours after the strong *Bise* event ended on 20 September, measurements at 10 points with 1-km spacing along transect T2, from South to North, were taken. The measured velocity field confirmed the existence of a cyclonic circulation in the center of the *Grand Lac* (Figures 7a, b).

In the proposed procedure, the center of each gyre is calculated by averaging the coordinates of the centers of the minimum $\mathrm{OW_N}$ zones at different depth layers. To take into account the uncertainty in selecting the location of each transect, the standard deviation of coordinates of minimum $\mathrm{OW_N}$ zones from the average transect was also calculated. It was ~ 1.8 km for September 2018. Therefore, measurements along two additional transects, T2R and T2L, were taken to cover the low velocity core zones (almost zero) surrounding the center. The velocity field for each transect is given in Figure 7c. The 3D velocity field shows a cyclonic gyre. The gyre velocity field penetrated down to ~15 m, limited by the strong thermal stratification in September (see Figure S1 for temperature profile at SHL2 near the center of CG1). The maximum horizontal water velocity reaches ~35 cm s^{-1} in the near-surface layer. The center of the cyclonic gyre can clearly be seen in all transects by the strong decrease in horizontal velocity.

In order to capture the gyre boundary and to determine the complete CG1 velocity field, 12 points with 1.5-km spacing were measured along transect T2H (see Figure 1b for location), from West to East on 22 September. For example, point 1 at the western end of the transect was clearly outside the gyre field because both the velocity magnitude and direction changed. Transect 2 (T2), from South to North was repeated. The field results (Figure 7d) confirmed the boundaries of CG1, which were

https://doi.org/10.5194/gmd-2022-104
Preprint. Discussion started: 19 July 2022

identified in the SAR image (see Figure 4a). Furthermore, the velocity field shows that the nearshore (South and North) currents are much stronger than currents at the East-West boundary of CG1, indicating that the nearshore bathymetry deforms/confines the gyre flow field.

An analysis similar to that of September 2018 discussed above was carried out for September 2019 and the results showed good agreement (Figure S3). Comparisons between the modeled and observed velocity fields for the September 2019 campaign are also given in Figure S5, again confirming the close resemblance between the results of field observations and the numerical modeling.

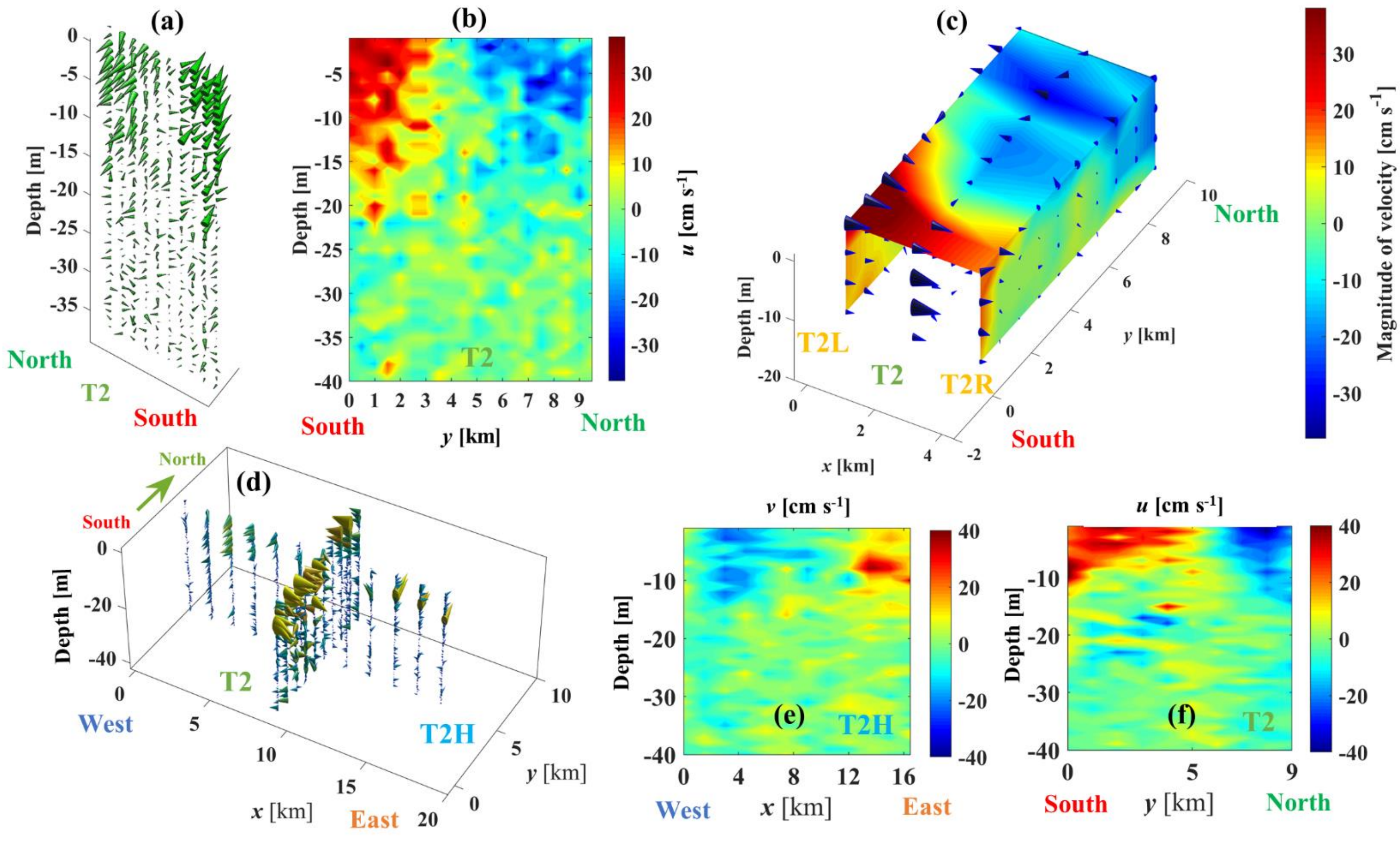

Figure 7. Measured current velocity field for sampling points along the selected transects (T) shown in Figure 1b for (a), (b) 20 September (c) 21 September (d)-(f) 22 September 2019. The coordinates of sampling points in T2 are the same in (a)-(d)

and (f). The colorbars indicate horizontal velocity in cm s^{-1}. Positive velocities are pointing eastward for transect T2, and northward for transect T2H. Positive velocities are pointing eastward for transect T2, and northward for transect T2H.

4.2.2 Observations of two- and three-gyre patterns

In most previous numerical studies on Lake Geneva, two basin-scale gyres (a dipole), located in the center of the deep *Grand Lac* basin were considered to be the main basin-scale circulation (Le Thi et al., 2012; Razmi et al., 2017). To confirm the existence of a dipole in Lake Geneva, field measurements were conducted from 23 to 25 October 2019 and from 24 to 26 November 2019 after strong *Bise* wind events occurred (Figure S4). However, the primary objective of the field campaign on 25 October and 25 November 2019 was to determine whether three large-scale gyres predicted by the EOF analysis (Figures 3, 4) exist in Lake Geneva.

The average wind direction during the *Bise* event in October 2019 was ~69° with a duration of 40 h, and was ~ 47° with a duration of 94 h in November 2019 (Figure S4). For the October 2019 campaign, two transects, T2 (western part) and T3 (eastern part) (Figure 1b), which consisted of 10 measurement points with 1-km spacing, were selected following the proposed procedure, but with different transect coordinates (e.g., T2) for each month. To confirm the existence of the third gyre in the eastern part of lake, CG2, two transects, T1 and T1H (see Figure 1b), each with eight points were selected. The distance between the T1H measurement points was 1.5 km in order to capture the CG2 boundary observed in the SAR image (Figure 4). In the 3D velocity field recorded during the October campaign at different transects (Figure 8), a dipole consisting of an anticyclonic gyre, AG, at transect T3, and a cyclonic gyre, CG1, at T2 is clearly evident. The maximum velocity at CG1 (22 cm s^{-1}) is stronger than at AG (15 cm s^{-1}), with the velocity field of AG penetrating into deeper layers. The 3D velocity field observed at T1 and T1H confirms the existence of the third cyclonic gyre (CG2) in the eastern part of Lake Geneva (Figure 8d). The CG2 velocity field penetrated down to nearly 20 m and the maximum horizontal water velocity reaches ~17 cm s^{-1} near the surface layer. The depth of the CG2 gyre is similar to that of CG1 and the magnitude of its velocity is comparable to AG.

To further confirm the existence of the three gyre pattern in Lake Geneva during weakly stratified months, measurements along the three transects, T1, T2, and T3 (Figure 1b), were carried out in November 2019, based on the EOF analysis for November 2018. During November, a different location for T3 was chosen because, compared to the October campaign, a different spatial pattern was observed in the EOF results (see Table S1). The transects T1 (eastern part), T2 (central part), and T3 (western part) were sampled on the same day, with 9, 10 and 8 points, respectively, each with a 1-km spacing. The measured 3D velocity fields reveal two cyclonic circulations at T1 and T2 and one anticyclonic circulation at T3 (Figure 8g). In contrast to the October campaign, the magnitude and depth of the velocity field at CG2 and CG1 are comparable. Comparisons between the modeled and observed velocity fields for October and November 2019 campaigns show good agreement (Figures S6 and S7 in SI).

https://doi.org/10.5194/gmd-2022-104
Preprint. Discussion started: 19 July 2022

Geoscientific Model Development
Discussions

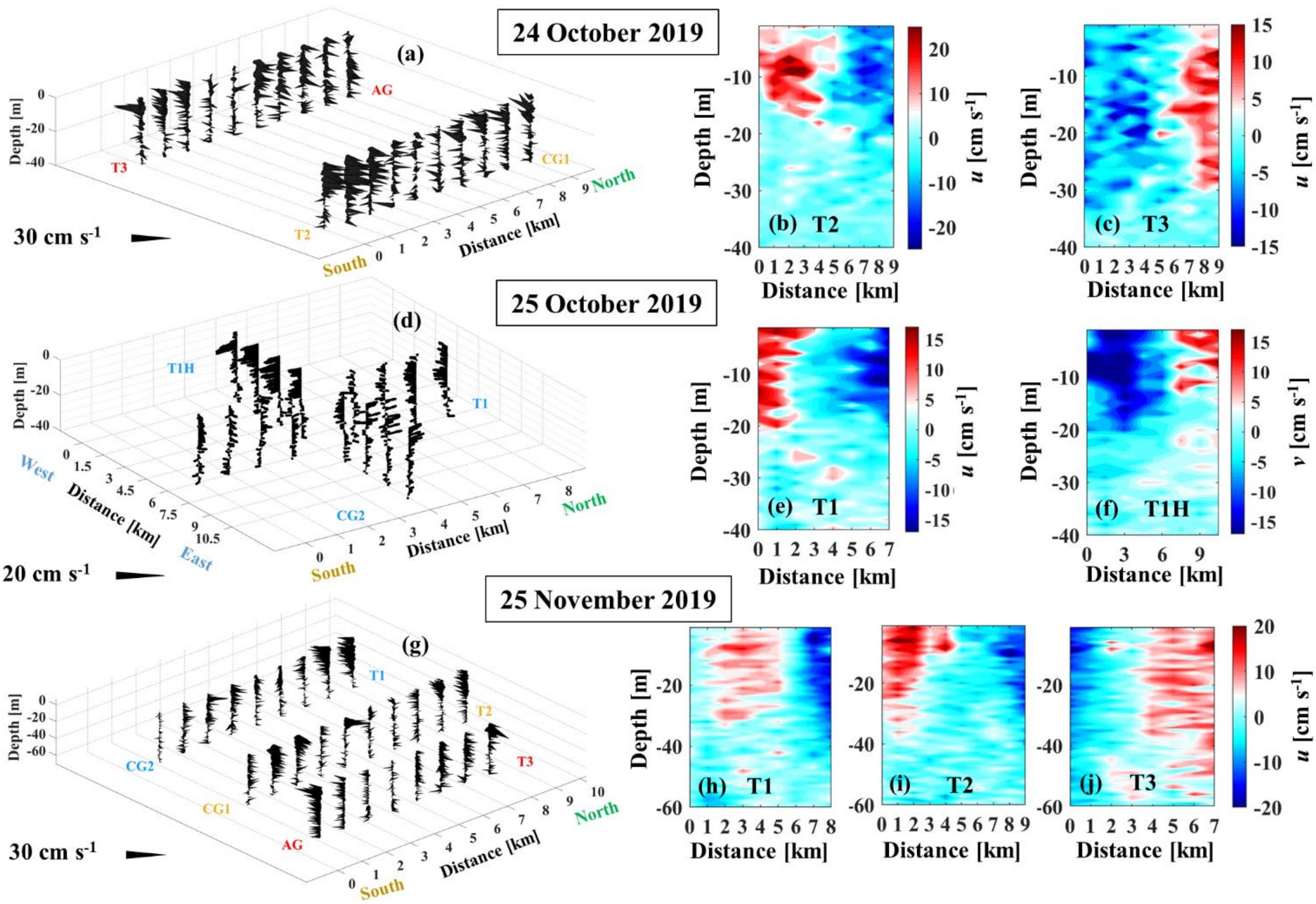

Figure 8. Field campaigns of October and November 2019: (a) the current velocity field (arrows) of gyres AG and CG1 and (b, c) the horizontal velocity, *u*, for sampling points along the selected transects (T) for the 24 October 2019 campaign. (d) The current velocity field of CG2 and (e,f) the horizontal components of velocity field, *u* and *v*, for sampling points along the selected transects for the 25 October 2019 campaign. (g) The current velocity field of AG, CG1 and CG2 and (h-j) the horizontal velocity, *u*, for sampling points along the selected transects for the November 2019 campaign. The colorbars indicates horizontal velocity in cm s^{-1}. Positive velocities are pointing eastward for transect T1, T2 and T3, and northward for transect T1H.

4.3 Detecting small eddies

Small Eddies (SE) have not yet been investigated in Lake Geneva. In the present study, smaller-sized coherent structures with negative OW_N values were detected in the vicinity of the basin-scale gyres or at coastal headlands (Figure 3). Two dominant and frequently occurring patterns of such eddies were selected in the EOF analysis for different months (Figures 9 and 10). The focus here was on eddies with a lifetime of several days, comparable to the lifetime of basin-scale gyres, i.e., SE1 and SE2 (see Figure 9c for location). In the SAR images, small eddies appear as radar-dark filaments wound into spirals. A close similarity between the patterns observed in the SAR data and numerical results is observed (cf. Figures 9 and 10). According to the numerical results, the rotation of SE1 is cyclonic and its diameter is of O(5) km during October 2019.

Such small-scale patterns cannot be adequately captured by velocity measurements at fixed points. Therefore, the ADCP was mounted on a small, boat-towed catamaran. Continuous vertical current profiles were measured along the preselected transects. SE1 was frequently observed by the proposed procedure during October 2018 and 2019 (not shown). A field campaign was conducted in October 2020 to investigate the vertical structure of SE1. Two transects, T4 and T5, were chosen based on EOF results and SAR images for the years 2018 and 2019. The horizontal lengths of T4 and T5 were ~8.5 and 3.5 km, respectively. The spatial resolution of the measured current profiles depends on the boat's speed (1.5-2 km/h). Velocity data were averaged every minute, which resulted in a 25-33 m spatial resolution along each transect. The numerical results and measured horizontal velocities at T4 and T5 are given in Figures 9e-h. A cyclonic circulation formed in the southwestern part of lake, and an anticyclonic circulation in the northwestern part (Figure 9d). There is a close match between the measured and modeled velocity fields (see Figure 8e, h). Field data indicate that the velocity field of SE1 extended to depths between 35-40 m, comparable to the depth of the anticyclonic gyre (AG) in this part of the lake measured during the October 2019 campaign.

Flow separation in the vicinity of headlands or baroclinicity due to favorable upwelling in the *Petit Lac* can also lead to the formation of a submesoscale eddy, such as SE2 (Figure 10). The dimensions of SE2 are generally smaller than those of SE1. However, SE2 is more frequently observed during certain months of year. For example, the signature of SE2 can be clearly observed in SAR images taken on 19 August 2018 and 7 November 2018 (Figure 10). The high-resolution numerical results confirm the presence of cold cyclonic eddies with the same dimensions for the same period (Figures 10b,d). The dimension of SE2 is of O(4 km). A field campaign on 3 September 2020 confirmed the existence of SE2. The simulated and measured velocity fields indicate a cyclonic circulation in the northwestern part of *Grand L*ac basin of Lake Geneva (Figures 10e, f). Field data also show that the SE2 velocity field can reach 20-m depth, which is 5-m deeper than the depth of the cyclonic circulation during the September 2019 campaign. Generally, such small eddies have a transient nature. However, eddies SE1 and SE2 are trapped between larger-scale gyres (Figure S6) or between boundaries and gyres, and remain at fixed locations for several days.

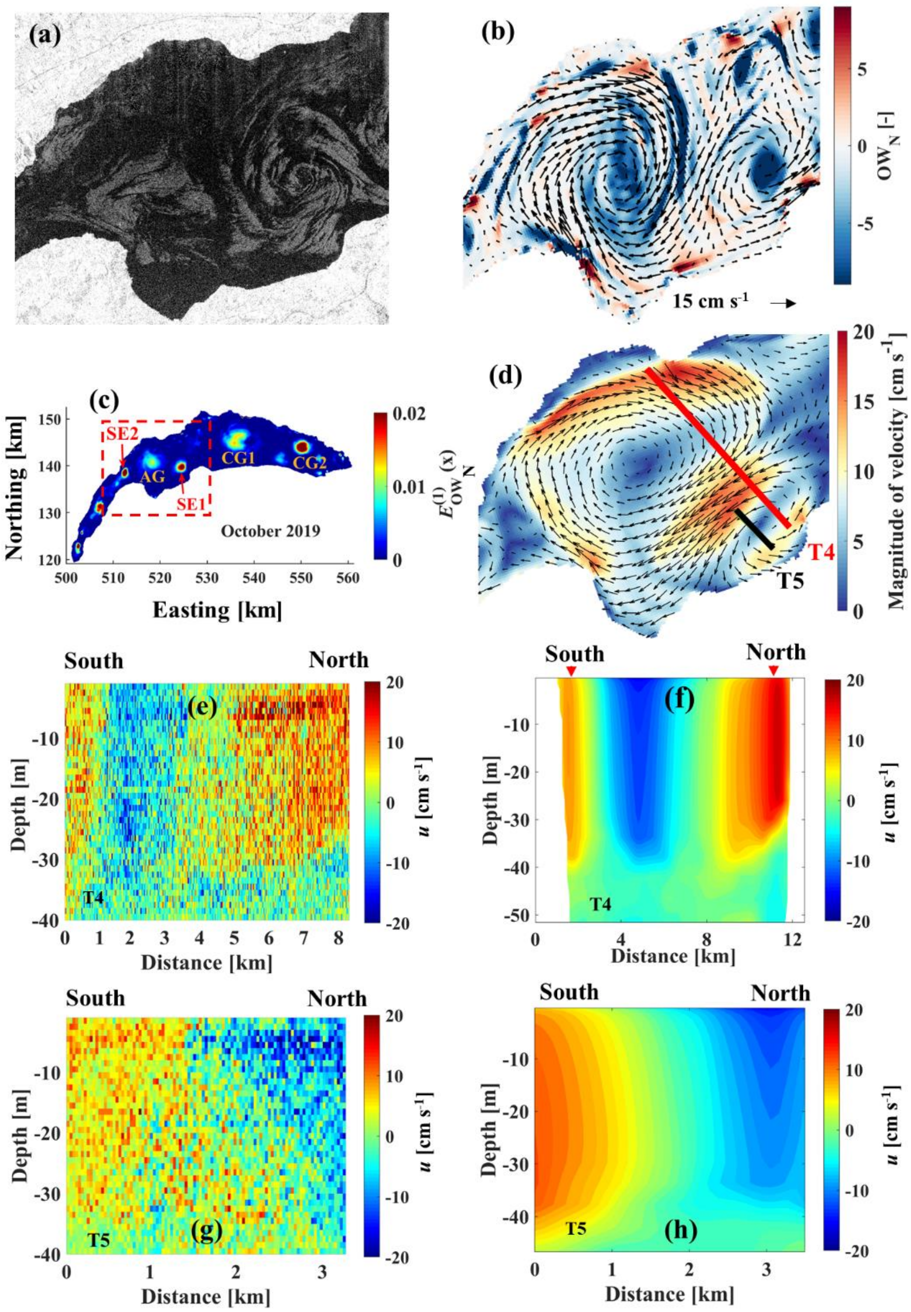

Figure 9. Evidence for the existence of submesoscale eddy (SE1). (a) Remote sensing evidence (SAR images, Sentinel-1) of SE1 for 27 October 2019. (b) Corresponding modeled surface velocity fields (small black arrows show sense of rotation) and OW parameter values shown by colors. (c) The first modes of EOF of the normalized OW_N parameter for October 2019 with large gyres AG1, CG1 and CG2 and small eddies SE1 and SE2. (d) Modeled surface velocity fields for 19 October 2020 and

https://doi.org/10.5194/gmd-2022-104
Preprint. Discussion started: 19 July 2022

Geoscientific Model Development
Discussions

selected transect locations (T4 and T5). (e) Measured horizontal current velocity profile along T4. (f) Corresponding modeled horizontal velocity along T4. (g) Measured horizontal current velocity profile along T5. Red dashed-lined rectangle in (c) indicates the location of zoom panels a), b) and d). Colorbars give the range of the parameters in the panels. Positive horizontal velocity in cm s^{-1} is pointing eastward.

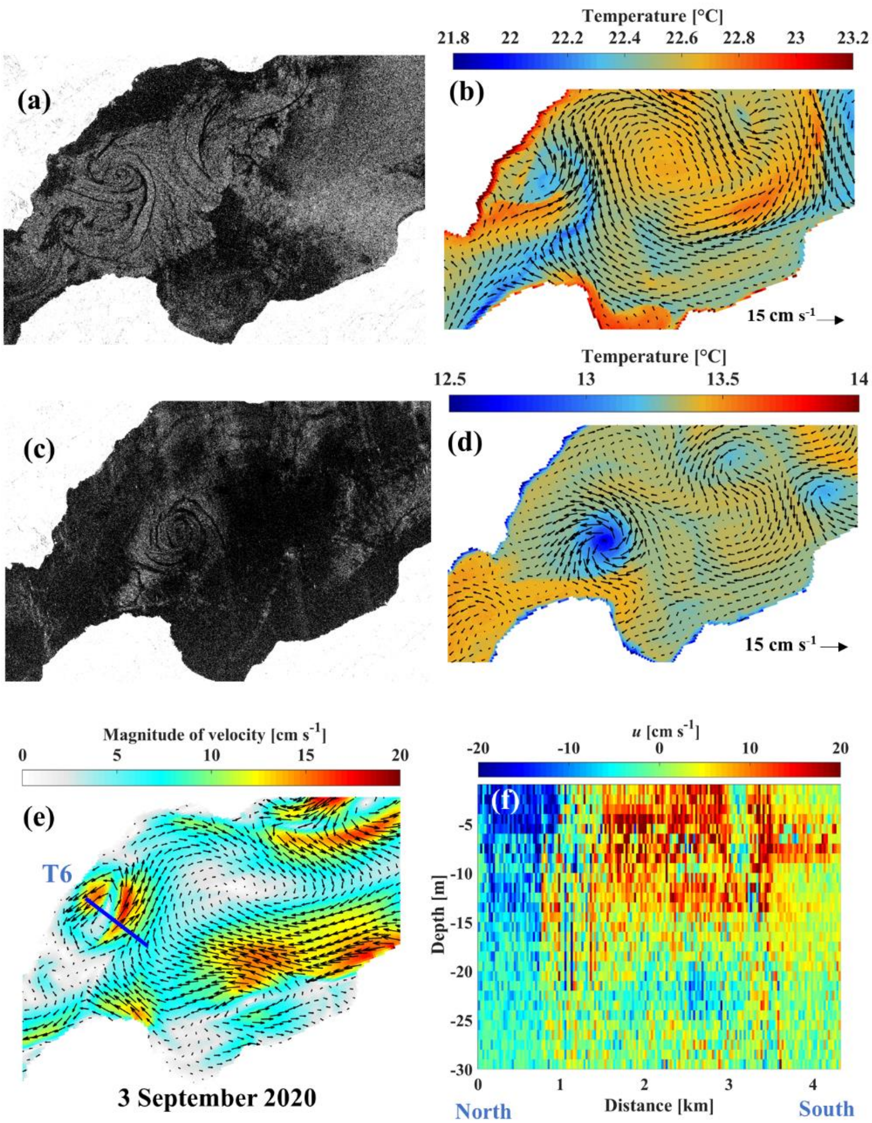

435

Figure 10. Evidence for the existence of submesoscale eddy (SE2). (a) Remote sensing evidence (SAR image, Sentinel-1) of SE2 for 19 August 2018. (b) Corresponding modeled surface velocity fields (small black arrows show sense of rotation) and temperature parameter values shown by colors. (c) SAR image of SE2 for 7 November 2018. (d) Corresponding modeled surface velocity fields and temperature for 7 November 2018. (e) The modeled surface velocity and selected transect (T6) for

https://doi.org/10.5194/gmd-2022-104
Preprint. Discussion started: 19 July 2022

field campaign on 3 September 2020. (f) Measured horizontal current velocity along T6. For location of these panels, see Figure 9c. Colorbars give the range of the parameters in the panels. Positive horizontal velocity in cm s^{-1} is pointing eastward.

5 Discussion

5.1 Procedure

Large scale gyres and eddies are important transport processes in large lakes allowing the rapid spreading of materials from the nearshore zone into the lake interior. The present study proposed a procedure that allows locating gyres and small eddies in a large lake and determining the details of their patterns. Its application to Lake Geneva has shown that a unique relationship exists between *Bise* wind forcing events and the resultant three-gyre pattern which is predictable and stable in space and time for a certain period after the forcing has ceased. The subsequent confirmation of the results by transect field measurements whose location and timing was based on the predicted pattern has demonstrated the feasibility and the robustness of the procedure. As a result, strategies for such field campaigns can be designed ensuring a high success rate. Without the information provided by this procedure, it is almost impossible to carry out such field campaigns, since the EOF results highlighted the complex nature of circulation patterns that exist in Lake Geneva.

5.2 Gyre pattern: Two or three gyres?

Numerical studies have shown that large-scale gyres contribute significantly to the transport of water masses and potential pollutants from the nearshore zone into the interior of the lake (Cimatoribus et al., 2019; Reiss et al., 2020). Particle tracking used in these studies indicated a rapid spreading of these water masses over large areas of the *Grand Lac* basin within a short time, once they were caught in gyres. Previous studies on Lake Geneva suggested that two basin-scale gyres located at the center of the deep *Grand Lac* basin drive the main basin-scale circulation (Le Thi et al., 2012; Razmi et al., 2017) and can have an impact on lake bio-chemical-physical interactions (Cotte and Vennemann, 2020). However, no field measurements were carried out to confirm the existence of a two-gyre pattern observed in these numerical simulation studies. In the present study, transect field measurements provided detailed evidence of these two gyres.

Furthermore, transect field measurements confirmed that a third gyre located in the eastern part of *Grand Lac* basin is as well developed as the other two gyres. Previously, modeling had suggested that this third gyre may be important for the rapid spreading of water masses and potential pollutants brought into the lake by the Rhône River, because its plume directly fed into this gyre (Lemmin, 2016). Generally, the signature of the cyclonic gyres, CG1 and CG2, in the center and eastern part of the lake, is more pronounced than that of the anticyclonic gyre, AG, in the west. The western part of lake is directly exposed to strong wind energy input, whereas the eastern parts are sheltered from strong wind (Rahaghi et al., 2019; Figure 5a).

https://doi.org/10.5194/gmd-2022-104
Preprint. Discussion started: 19 July 2022

Based on the EOF analysis in the proposed procedure, it was possible in the present study to extend previous individual gyre investigations into a statistically significant gyre pattern. Thus, the link of this pattern to forcing was made evident and indicated that the location of gyre centers and the duration of the gyre pattern only changed slightly between events.

5.3 Forcing: Importance of spatial heterogeneity

The dominant role of wind as the primary force in gyre formation, the impact of stratification and Coriolis forcing, and the importance of surface heating and cooling in driving or enhancing gyre flows have recently been highlighted (Hogg and Gayen, 2020). The spatial pattern of the net heat flux suggests that the heterogeneity between heating and cooling in the eastern part of the lake is more significant than in the western part (Figure 5b). This agrees with findings of spatial heat flux variability by Rahaghi et al., (2019). The variability may impact on the strength of gyre flows in the eastern part of Lake Geneva. Further research is needed in order to quantify the role of differential surface buoyancy fluxes on the strength of cyclonic gyres in the eastern part of lake, particularly during summertime when diurnal heating and cooling are stronger. As shown in Figure 8, the depth influenced by the gyre field (AG) in the western part of the lake is greater than the depths influenced by CG1 and CG2 located in the center and eastern part of the lake for the November and October campaigns. The gyre velocity is constrained by the thermocline depth, as previously discussed. The thermocline depth can also be affected by the spatial heterogeneity of atmospheric forcing and gyre motions. Forcing by wind stress, the primary source of energy for mixing the water column, is more pronounced in the western part (Figures 5a; S3, and S4 in SI). Consequently, a deeper mixed layer would be expected in the western part of the lake. The lower velocity of gyre flow in the western part of the lake can be attributed to the fact that the wind energy can penetrate into deeper layers due to a deeper thermocline, whereas it is confined by a shallower thermocline in the eastern part of lake. As a result, the maximum velocity field of CG1 and CG2 is generally greater than AG.

5.4 Small eddies

The spatial pattern in the OW_N computed for October 2019 is slightly different than that of September 2019, i.e., a strong smaller-scale cyclonic circulation (SE1) exists near gyre AG in the western part of the lake (Figure 9). Small eddies, with approximately the size of the Rossby radius, are predicted by the numerical modeling and are important in the mixing and transport of lake water masses. They were most often observed shedding from headlands, trapped between basin-scale gyres, as well as being ejected from bays (Razmi et al., 2017). Although it is beyond the scope of this study to investigate the origin of small eddies, it was demonstrated that the proposed procedure can detect and locate them correctly, as was confirmed by transect field measurements. Small eddies can play an important role with respect to sea and ocean turbulence, stratification and primary production (Mahadevan, 2016). Generally, such small eddies are expected to be transient in nature. However, eddies SE1 and SE2 were trapped between large-scale gyres or between boundaries and gyres, hardly lost any strength and remained active at fixed locations for several days, comparable to the lifetime of large-scale gyres.

https://doi.org/10.5194/gmd-2022-104
Preprint. Discussion started: 19 July 2022

The results of this study suggest that by applying the proposed procedure, it is possible to develop strategies for detailed transect field studies that can be extended to bio-geo-chemical parameters which may have ecological importance.

6 Summary and conclusions

In order to advance the understanding of water mass movement dynamics in large lakes, it is essential to determine the contribution of basin-scale gyres and (sub)mesoscale eddies. In particular, it is important to know to what extent the flow field generated by gyres and eddies observed during a single forcing event is "typical" and thus key to the longterm development of the lake flow field. Unfortunately, at present, a procedure that would allow identifying and tracking basin-scale and mesoscale water mass movements in a wider lake database does not exist. We therefore developed a procedure combining high-resolution 3D numerical simulations, the Okubo-Weiss (OW) parameter and EOF analysis that can provide direct evidence of the existence of cyclonic (counterclockwise) and anticyclonic (clockwise) rotating basin-scale gyres and meso-scale eddies in large lakes. Its feasibility and robustness was assessed and confirmed by transect field measurements taken in Lake Geneva.

The gyre flow field is characterized by a coherent pattern of the normalized Okubo-Weiss parameter, OW_N, in different layers of the lake, as was detected by the EOF analysis. The results showed a clear link between strong large-scale wind events and the computed spatial patterns in the first mode of the EOF analysis. The procedure allows detecting the location of gyre centers where almost zero horizontal velocity zones indicate the occurrence of pelagic upwelling or downwelling which has a great impact on the biological-chemical-physical development of large lake ecological systems (Troitskaya et al., 2015).

Furthermore, field observations confirmed for the first time that three persistent gyres, two cyclonic gyres and one anticyclonic gyre, formed after strong *Bise* wind events, as was predicted by the proposed procedure. According to the EOF analysis, the horizontal gyre motion is mainly responsive to the wind stress, whereas the depth of the gyre flow field mainly depends on thermocline depth.

Field observations during October and November 2019 demonstrated that the depth of gyre penetration is greater in the western (anticyclonic gyre) than in the eastern part of the lake (cyclonic gyres). The spatial inhomogeneities in external forcing can lead to significant spatial variability of the gyre velocity field in the western and eastern parts of Lake Geneva.

The proposed procedure can also detect (sub)mesoscale eddies, if the resolution of the numerical modeling grid is high enough. These eddies were predominantly cyclonic, and their diameters were of O(4-5 km). They may occur due to flow separation in the vicinity of headlands and embayments. These eddies are transient, but if trapped between larger-scale gyres, they can remain at a fixed location for several days, and can have a lifetime comparable to basin-scale gyres. Their patterns were confirmed by field campaigns designed following the proposed procedure.

This study highlighted the significance of 3D processes in large lakes, thus indicating that 1D concepts cannot adequately describe the dynamics in such lakes. Further research is required to investigate gyre/eddy-formation mechanisms and the role that eddies and large basin-scale gyres play in the interaction of biological-chemical-physical processes. They may rapidly spread materials entering the lake in the nearshore zone into the whole lake, and thus affect the long-term ecological system

https://doi.org/10.5194/gmd-2022-104
Preprint. Discussion started: 19 July 2022

Geoscientific Model Development Discussions

development of large lakes. Although the feasibility and robustness of the proposed procedure was assessed in Lake Geneva, it can be applied to any large lake with a comparable data base, since it is based on universally valid concepts. It is a powerful tool for designing strategies for detailed field studies and will allow new types of field measurements that can contribute to advancing the understanding of large lake dynamics.

Acknowledgments

This research was supported by the Swiss National Science Foundation (SNSF Grant 178866). The spatiotemporal meteorological data were provided by the Federal Office of Meteorology and Climatology in Switzerland (MeteoSwiss). We also extend our appreciation to the Commission Internationale pour la Protection des Eaux du Léman (CIPEL) for in situ temperature measurements. Water temperature profiles were collected at the CIPEL SHL2 station for 2018-2019 by the Eco-Informatics ORE INRA Team at the French National Institute for Agricultural Research (SOERE OLA-IS, INRA Thonon-les-Bains, France).

Data availability

The SAR images used in this study are based on Sentinel-1 raw data, which are made available by the ESA and can freely be downloaded from the ESA's Sentinel data hub (https://scihub.copernicus.eu/). The three-dimensional model used in this study is based on the MIT General Circulation Model (MITgcm, http://mitgcm.org/, https://doi.org/10.1029/96JC02775), which is publicly available. The in situ data and numerical configurations supporting the findings of this study are available online at https://github.com/mahmoodziabar/Data-for-GMD-paper.git.

Author contributions

SMHZ planned the field campaign; SMHZ, FS, and MF performed the measurements; SMHZ analyzed the data; SMHZ wrote the manuscript draft; DAB and UL reviewed and edited the manuscript.

Competing interests

The authors declare that they have no conflict of interest.

https://doi.org/10.5194/gmd-2022-104
Preprint. Discussion started: 19 July 2022

References

Akitomo, K., Kurogi, M., and Kumagai, M.: Numerical study of a thermally induced gyre system in Lake Biwa, Limnology, 5(2), 103-114, https://doi.org/10.1007/s10201-004-0122-9, 2004.

Bai, X., Wang, J., Schwab, D. J., Yang, Y., Luo, L., Leshkevich, G. A., and Liu, S.: Modeling 1993–2008 climatology of seasonal general circulation and thermal structure in the Great Lakes using FVCOM, Ocean Model., 65, 40-63. https://doi.org/10.1016/j.ocemod.2013.02.003, 2013.

Baracchini, T., Wüest, A., and Bouffard, D.: Meteolakes: an operational online three-dimensional forecasting platform for lake hydrodynamics, Water Res., 172, 115529, https://doi.org/10.1016/j.watres.2020.115529, 2020.

Baracchini, T., Chu, P. Y., Šukys, J., Lieberherr, G., Wunderle, S., Wüest, A., and Bouffard, D.: Data assimilation of in situ and satellite remote sensing data to 3D hydrodynamic lake models: a case study using Delft3D-FLOW v4.03 and OpenDA v2.4, Geosci. Model Dev., 13, 1267–1284, https://doi.org/10.5194/gmd-13-1267-2020, 2020.

Beletsky, D., Hawley, N., and Rao, Y. R.: Modeling summer circulation and thermal structure of Lake Erie, J. Geophys. Res. Oceans., 118(11), 6238-6252, https://doi.org/10.1002/2013JC008854, 2013.

Beletsky, D., Saylor, J. H., and Schwab, D. J.: Mean circulation in the Great Lakes. J. Great Lakes Res., 25(1), 78-93, https://doi.org/10.1016/S0380-1330(99)70718-5, 1999.

Beletsky, D., and Schwab, D.: Climatological circulation in Lake Michigan. Geophys. Res. Lett., 35(21), L21604, https://doi.org/10.1029/2008GL035773, 2008.

Bennett, J. R.: On the dynamics of wind-driven lake currents, J. Phys. Oceanogr., 4(3), 400-414, https://doi.org/10.1175/1520-0485(1974)004<0400:OTDOWD>2.0.CO;2, 1974.

Bennington, V., McKinley, G. A., Kimura, N., and Wu, C. H.: General circulation of Lake Superior: Mean, variability, and trends from 1979 to 2006. J. Geophys. Res.: Oceans, 115(C12), C12015. https://doi.org/10.1029/2010JC006261, 2010.

Birchfield, G. E.: Horizontal transport in a rotating basin of parabolic depth profile, J. Geophys. Res., 72(24), 6155-6163, https://doi.org/10.1029/JZ072i024p06155, 1967.

Chang, Y. L., and Oey, L. Y.: Analysis of STCC eddies using the Okubo–Weiss parameter on model and satellite data, Ocean Dyn., 64(2), 259-271, https://doi.org/10.1007/s10236-013-0680-7, 2014.

Cimatoribus, A. A., Lemmin, U., Bouffard, D., and Barry, D. A.: Nonlinear dynamics of the nearshore boundary layer of a large lake (Lake Geneva), J. Geophys. Res.: Oceans, 123(2), 1016-1031, https://doi.org/10.1002/2017JC013531, 2018.

Cimatoribus, A. A., Lemmin, U., and Barry, D. A.: Tracking Lagrangian transport in Lake Geneva: A 3D numerical modeling investigation. Limnol. Oceanogr., 64(3), 1252-1269. https://doi.org/10.1002/lno.11111, 2019.

CIPEL: Rapports sur les études et recherches entreprises dans le bassin lémanique, Campagne 2018, Commission internationale pour la protection des eaux du Léman (CIPEL), Nyon, Switzerland. https://www.cipel.org/wp-content/uploads/2018/04/RapportScientifique_camp_2016_VF.pdf, 2019.

https://doi.org/10.5194/gmd-2022-104
Preprint. Discussion started: 19 July 2022

Corman, J.R., McIntyre, P.B., Kuboja, B., Mbemba, W., Fink, D., Wheeler, C.W., Gans, C., Michel, E., and Flecker, A. S.: Upwelling couples chemical and biological dynamics across the littoral and pelagic zones of Lake Tanganyika, East Africa, Limnol. Oceanogr., 55(1), 214-224, https://doi.org/10.4319/lo.2010.55.1.0214, 2010.

Cotte, G., and Vennemann, T. W.: Mixing of Rhône River water in Lake Geneva: Seasonal tracing using stable isotope composition of water, J. Great Lakes Res., 46(4), 839-849, https://doi.org/10.1016/j.jglr.2020.05.015, 2020.

Csanady, G. T.: Wind-induced barotropic motions in long lakes, J. Phys. Oceanogr., 3(4), 429-438, https://doi.org/10.1175/1520-0485(1973)003<0429:WIBMIL>2.0.CO;2, 1973.

Csanady, G. T.: Hydrodynamics of large lakes, Annu. Rev. Fluid Mech., 7(1), 357-386, https://doi.org/10.1146/annurev.fl.07.010175.002041, 1975.

Cushman-Roisin, B., and Beckers, J. M.: Introduction to geophysical fluid dynamics: physical and numerical aspects, Academic press, 2011.

DiGiacomo, P. M., and Holt, B.: Satellite observations of small coastal ocean eddies in the Southern California Bight, J. Geophys. Res.: Oceans., 106(C10), 22521-22543, https://doi.org/10.1029/2000JC000728, 2001.

Dokken, S. T., and Wahl, T.: Observations of spiral eddies along the Norwegian Coast in ERS SAR images, http://hdl.handle.net/20.500.12242/1449, 1996.

Donelan, M. A., and Pierson Jr, W. J.: Radar scattering and equilibrium ranges in wind-generated waves with application to scatterometry, J. Geophys. Res.: Oceans, 92(C5), 4971-5029, https://doi.org/10.1029/JC092iC05p04971, 1987.

Elhmaïdi, D., Provenzale, A., and Babiano, A.: Elementary topology of two-dimensional turbulence from a Lagrangian viewpoint and single-particle dispersion, J. Fluid Mech., 257, 533-558, https://doi.org/10.1017/S0022112093003192, 1993.

Gao, Y., Guan, C., Sun, J., and Xie, L.: A wind speed retrieval model for Sentinel-1A EW mode cross-polarization images, Remote Sens., 11(2), 153, https://doi.org/10.3390/rs11020153, 2019.

Henson, S. A., and Thomas, A. C.: A census of oceanic anticyclonic eddies in the Gulf of Alaska. Deep Sea Res., Part I., 55(2), 163-176, https://doi.org/10.1016/j.dsr.2007.11.005, 2008.

Hogg, A. M., and Gayen, B.: Ocean gyres driven by surface buoyancy forcing, Geophys. Res. Lett., 47(16), e2020GL088539, https://doi.org/10.1029/2020GL088539, 2020.

Hui, Y., Farnham, D. J., Atkinson, J. F., Zhu, Z., and Feng, Y.: Circulation in Lake Ontario: numerical and physical model analysis, J. Hydraul. Eng., 147(8), 05021004, https://doi.org/10.1061/(ASCE)HY.1943-7900.0001908, 2021.

Ishikawa, K., Kumagai, M., Vincent, W. F., Tsujimura, S., and Nakahara, H.: Transport and accumulation of bloom-forming cyanobacteria in a large, mid-latitude lake: the gyre-Microcystis hypothesis, Limnology, 3(2), 87-96, https://doi.org/10.1007/s102010200010, 2002.

Isern-Fontanet, J., Font, J., García-Ladona, E., Emelianov, M., Millot, C., and Taupier-Letage, I.: Spatial structure of anticyclonic eddies in the Algerian basin (Mediterranean Sea) analyzed using the Okubo–Weiss parameter, Deep Sea Res., Part II, 51(25-26), 3009-3028, https://doi.org/10.1016/j.dsr2.2004.09.013, 2004.

Isern-Fontanet, J., García-Ladona, E., and Font, J.: Vortices of the Mediterranean Sea: An altimetric perspective. J. Phys. Oceanogr., 36(1), 87-103, https://doi.org/10.1175/JPO2826.1, 2006.

Ji, Z. G., and Jin, K. R.: Gyres and seiches in a large and shallow lake, J. Great Lakes Res., 32(4), 764-775, https://doi.org/10.3394/0380-1330(2006)32[764:GASIAL]2.0.CO;2, 2006.

Johannessen, J. A., Kudryavtsev, V., Akimov, D., Eldevik, T., Winther, N., and Chapron, B.: On radar imaging of current features: 2. Mesoscale eddy and current front detection, J. Geophys. Res.: Oceans, 110(C7), C07017, https://doi.org/10.1029/2004JC002802, 2005.

Johannessen, J. A., Shuchman, R. A., Digranes, G., Lyzenga, D. R., Wackerman, C., Johannessen, O. M., and Vachon, P. W.: Coastal ocean fronts and eddies imaged with ERS 1 synthetic aperture radar. J. Geophys. Res.: Oceans, 101(C3), 6651-6667, https://doi.org/10.1029/95JC02962, 1996.

Karimova, S.: Spiral eddies in the Baltic, Black and Caspian seas as seen by satellite radar data, Adv. Space Res., 50(8), 1107-1124, https://doi.org/10.1016/j.asr.2011.10.027, 2012.

Laval, B. E., Imberger, J., and Findikakis, A. N.: Dynamics of a large tropical lake: Lake Maracaibo, Aquat. Sci., 67(3), 337-349, https://doi.org/10.1007/s00027-005-0778-1, 2005.

Le Thi, A. D., De Pascalis, F., Umgiesser, G., and Wildi, W.: Structure thermique et courantologie du Léman (Thermal structure and circulation patterns of Lake Geneva), Arch. Sci., 65, 65-80, https://archive-ouverte.unige.ch/unige:27717, 2012.

Lemmin, U., Mortimer, C. H., and Bäuerle, E.: Internal seiche dynamics in Lake Geneva, Limnol. Oceanogr., 50(1), 207-216, https://doi.org/10.4319/lo.2005.50.1.0207, 2005.

Lemmin, U.: Insights into the dynamics of the deep hypolimnion of Lake Geneva as revealed by long-term temperature, oxygen, and current measurements, Limnol. Oceanogr., 65(9), 2092-2107, https://doi.org/10.1002/lno.11441, 2020.

Lemmin, U. Mouvements des masses d'eau (Water mass movement), In: Lemmin U. (ed.), Dans les abysses du Léman (Descent into the abyss of Lake Geneva), Presses Polytechniques et Universitaires Romandes (PPUR), Switzerland. ISBN: 978-2-88915-105-9, 2016.

Lemmin, U., and D'Adamo, N.: Summertime winds and direct cyclonic circulation: Observations from Lake Geneva, Ann. Geophys, 14(11), 1207-1220, https://doi.org/10.1007/s00585-996-1207-z, 1996.

Lin, S., Boegman, L., Shan, S., and Mulligan, R.: An automatic lake-model application using near-real-time data forcing: development of an operational forecast workflow (COASTLINES) for Lake Erie, Geosci. Model Dev., 15, 1331–1353, https://doi.org/10.5194/gmd-15-1331-2022, 2022.

Liu, F., Zhou, H., and Wen, B.: DEDNet: Offshore eddy detection and location with HF radar by deep learning, Sensors, 21(1), 126, https://doi.org/10.3390/s21010126, 2020.

McKinney, P., Holt, B., and Matsumoto, K.: Small eddies observed in Lake Superior using SAR and sea surface temperature imagery, J. Great Lakes Res., 38(4), 786-797. https://doi.org/10.1016/j.jglr.2012.09.023, 2012.

McWilliams, J. C.: The emergence of isolated coherent vortices in turbulent flow, J. Fluid Mech., 146, 21-43, https://doi.org/10.1017/S0022112084001750, 1984.

Mahadevan, A.: The impact of submesoscale physics on primary productivity of plankton, Ann. Rev. Mar. Sci., 8, 161-184, https://doi.org/10.1146/annurev-marine-010814-015912, 2016.

Mao, M., and Xia, M.: Monthly and episodic dynamics of summer circulation in Lake Michigan, J. Geophys. Res.: Oceans., 125(6), e2019JC015932, https://doi.org/10.1029/2019JC015932, 2020.

Marmorino, G. O., Holt, B., Molemaker, M. J., DiGiacomo, P. M., and Sletten, M. A.: Airborne synthetic aperture radar observations of "spiral eddy" slick patterns in the Southern California Bight, J. Geophys. Res.: Oceans., 115(C5), C05010, https://doi.org/10.1029/2009JC005863, 2010.

Marshall, J., Adcroft, A., Hill, C., Perelman, L., and Heisey, C.: A finite-volume, incompressible Navier Stokes model for studies of the ocean on parallel computers, J. Geophys. Res.: Oceans., 102(C3), 5753-5766, https://doi.org/10.1029/96JC02775, 1997.

Moran, M. S., Hymer, D. C., Qi, J., and Kerr, Y.: Comparison of ERS-2 SAR and Landsat TM imagery for monitoring agricultural crop and soil conditions, Remote Sens. Environ., 79(2-3), 243-252, https://doi.org/10.1016/S0034-4257(01)00276-0, 2002.

Nõges, T., and Kangro, K.: Primary production of phytoplankton in a strongly stratified temperate lake, Hydrobiologia, 547(1), 105-122, https://doi.org/10.1007/1-4020-4363-5_10, 2005.

Okubo, A.: Horizontal dispersion of floatable particles in the vicinity of velocity singularities such as convergences, Deep-Sea Res. Oceanogr. Abstr., 17(3), 445-454, https://doi.org/10.1016/0011-7471(70)90059-8, 1970

Ostrovsky, I., and Sukenik, A.: Spatial heterogeneity of biogeochemical parameters in a subtropical lake, In Monitoring and Modelling Lakes and Coastal Environments, Springer, Dordrecht, https://doi.org/10.1007/978-1-4020-6646-7_6, 2008.

Pasquero, C., Provenzale, A., and Babiano, A.: Parameterization of dispersion in two-dimensional turbulence, J. Fluid Mech., 439, 279-303, https://doi.org/10.1017/S0022112001004499, 2001.

Perroud, M., Goyette, S., Martynov, A., Beniston, M., and Annevillec, O.: Simulation of multiannual thermal profiles in deep Lake Geneva: A comparison of one-dimensional lake models, Limnol. Oceanogr., 54(5), 1574-1594, https://doi.org/10.4319/lo.2009.54.5.1574, 2009.

Pickett, R.L., and Rao, D.B.: One-and two-gyre circulations in homogeneous lakes. International Field Year for the Great Lakes Bulletin 19, 45-49, U.S. Dept. of Commerce, National Oceanic and Atmospheric Administration, Rockville, Maryland. https://play.google.com/books/reader?id=AtZ918jAK10C&hl=en_GB&pg=GBS.PA45, 1977.

Qazi, W. A., Emery, W. J., and Fox-Kemper, B.: Computing ocean surface currents over the coastal California current system using 30-min-lag sequential SAR images, IEEE Trans. Geosci. Electron, 52(12), 7559-7580, https://doi.org/10.1109/TGRS.2014.2314117, 2014.

Rahaghi, A. I., Lemmin, U., Cimatoribus, A., Bouffard, D., Riffler, M., Wunderle, S., and Barry, D. A.: Improving surface heat flux estimation for a large lake through model optimization and two-point calibration: The case of Lake Geneva, Limnol. Oceanogr.: Methods, 16(9), 576-593, https://doi.org/10.1002/lom3.10267, 2018.

Rahaghi, A. I., Lemmin, U., Cimatoribus, A. A., and Barry, D. A.: The importance of systematic spatial variability in the surface heat flux of a large lake: A multiannual analysis for Lake Geneva, Water Resour. Res., 55(12), 10248-10267, https://doi.org/10.1029/2019WR024954, 2019.

Ralph, E. A.: Scales and structures of large lake eddies, Geophys. Res. Lett., 29(24), 30-1. https://doi.org/10.1029/2001GL014654, 2002.

Rao, D. B., and Murty, T. S.: Calculation of the steady state wind-driven circulations in Lake Ontario, Arch. Meteorol. Geophys.Bioklimatol., A., 19(2), 195-210, https://doi.org/10.1007/BF02249005, 1970.

Razmi, A. M., Barry, D. A., Bakhtyar, R., Le Dantec, N., Dastgheib, A., Lemmin, U., and Wüest, A.: Current variability in a wide and open lacustrine embayment in Lake Geneva (Switzerland), J. Great Lakes Res., 39(3), 455-465, https://doi.org/10.1016/j.jglr.2013.06.011, 2013.

Razmi, A. M., Lemmin, U., Bouffard, D., Wüest, A., Uittenbogaard, R. E., and Barry, D. A.: Gyre formation in open and deep lacustrine embayments: the example of Lake Geneva, Switzerland, Environ. Fluid Mech., 17(3), 415-428. https://doi.org/10.1007/s10652-016-9494-8, 2017.

Reiss, R. S., Lemmin, U., Cimatoribus, A. A., and Barry, D. A.: Wintertime coastal upwelling in Lake Geneva: An efficient transport process for deepwater renewal in a large, deep lake, J. Geophys. Res.: Oceans, *125*(8), e2020JC016095, https://doi.org/10.1029/2020JC016095, 2020.

Schwab, D. J., and Beletsky, D.: Relative effects of wind stress curl, topography, and stratification on large-scale circulation in Lake Michigan, J. Geophys. Res.: Oceans, 108(C2), 3044, https://doi.org/10.1029/2001JC001066, 2003.

Shilo, E., Ashkenazy, Y., Rimmer, A., Assouline, S., Katsafados, P., and Mahrer, Y.: Effect of wind variability on topographic waves: Lake Kinneret case, J. Geophys. Res.: Oceans, 112(C12), https://doi.org/10.1029/2007JC004336, 2007.

Simons, T. J.: Circulation models of lakes and inland seas, Can. Bull. Fish. Aquat. Sci., 203**,** 146, 1980.

Souza, J. M. A. C., de Boyer Montégut, C., and Le Traon, P. Y.: Comparison between three implementations of automatic identification algorithms for the quantification and characterization of mesoscale eddies in the South Atlantic Ocean, Ocean Sci., 7(3), 317-334, https://doi.org/10.5194/os-7-317-2011, 2011.

Steissberg, T. E., Hook, S. J., and Schladow, S. G.: Measuring surface currents in lakes with high spatial resolution thermal infrared imagery, Geophys. Res. Lett., 32(11), L11402, https://doi.org/10.1029/2005GL022912, 2005.

Troitskaya, E., Blinov, V., Ivanov, V., Zhdanov, A., Gnatovsky, R., Sutyrina, E., and Shimaraev, M.: Cyclonic circulation and upwelling in Lake Baikal, Aquat. Sci., 77(2), 171-182, https://doi.org/10.1007/s00027-014-0361-8, 2015.

Umlauf, L., and Lemmin, U.: Interbasin exchange and mixing in the hypolimnion of a large lake: The role of long internal waves, Limnol. Oceanogr., 50(5), 1601-1611, https://doi.org/10.4319/lo.2005.50.5.1601, 2005.

Voudouri, A., Avgoustoglou, E., and Kaufmann, P.: Impacts of observational data assimilation on operational forecasts, Perspectives on atmospheric sciences, 143-149, Springer, Cham, https://doi.org/10.1007/978-3-319-35095-0_21, 2017.

Verburg, P., Antenucci, J. P., and Hecky, R. E.: Differential cooling drives large-scale convective circulation in Lake Tanganyika, Limnol. Oceanogr., 56(3), 910-926, https://doi.org/10.4319/lo.2011.56.3.0910, 2011.

https://doi.org/10.5194/gmd-2022-104
Preprint. Discussion started: 19 July 2022

Geoscientific Model Development
Discussions

Wang, B., and An, S. I.: A method for detecting season-dependent modes of climate variability: S-EOF analysis, Geophys. Res. Lett., 32(15), L15710, https://doi.org/10.1029/2005GL022709, 2005.

Wang, C., Tandeo, P., Mouche, A., Stopa, J.E., Gressani, V., Longepe, N., Vandemark, D., Foster, R.C., and Chapron, B.: Classification of the global Sentinel-1 SAR vignettes for ocean surface process studies, Remote Sens. Environ., 234, 111457. https://doi.org/10.1016/j.rse.2019.111457, 2019.

Wanner, H., and Furger, M.: The Bise—Climatology of a regional wind north of the Alps, Physics Meteorol. Atmos. Phys., 43(1), 105-115, https://doi.org/10.1007/BF01028113, 1990.

Weiss, J.: The dynamics of enstrophy transfer in two-dimensional hydrodynamics, Phys. D: Nonlinear Phenom., 48(2-3), 273-294, https://doi.org/10.1016/0167-2789(91)90088-Q, 1991.

Wu, T., Qin, B., Huang, A., Sheng, Y., Feng, S., and Casenave, C.: Reconsideration of wind stress, wind waves, and turbulence in simulating wind-driven currents of shallow lakes in the Wave and Current Coupled Model (WCCM) version 1.0, Geosci. Model Dev., 15(2), 745-769, https://doi.org/10.5194/gmd-15-745-2022, 2022.

Xiu, P., Chai, F., Shi, L., Xue, H., and Chao, Y.: A census of eddy activities in the South China Sea during 1993–2007, J. Geophys. Res.: Oceans., 115(C3), C03012, https://doi.org/10.1029/2009JC005657, 2010.

Yamaguchi, S., and Kawamura, H.: SAR-imaged spiral eddies in Mutsu Bay and their dynamic and kinematic models, J. Oceanogr., 65(4), 525-539, https://doi.org/10.1007/s10872-009-0045-5, 2009.

Zhan, S., Beck, R. A., Hinkel, K. M., Liu, H., and Jones, B. M.: Spatio-temporal analysis of gyres in oriented lakes on the Arctic Coastal Plain of northern Alaska based on remotely sensed images, Remote Sens., 6(10), 9170-9193, https://doi.org/10.3390/rs6109170, 2014.